

DEVELOPMENT OF AN AXISYMMETRIC, TURBULENT AND
UNSTRUCTURED NAVIER-STOKES SOLVER

A THESIS SUBMITTED TO
THE GRADUATE SCHOOL OF NATURAL AND APPLIED SCIENCES
OF
MIDDLE EAST TECHNICAL UNIVERSITY

BY

MUSTAFA AKDEMİR

IN PARTIAL FULFILLMENT OF THE REQUIREMENTS
FOR
THE DEGREE OF MASTER OF SCIENCE
IN
MECHANICAL ENGINEERING

MAY 2010

Approval of the thesis:

DEVELOPMENT OF AN AXISYMMETRIC, TURBULENT AND UNSTRUCTURED NAVIER-STOKES SOLVER

submitted by **MUSTAFA AKDEMİR**, in partial fulfillment of the requirements for the degree of **Master of Science in Mechanical Engineering Department, Middle East Technical University** by,

Prof. Dr. Canan ÖZGEN
Dean, Graduate School of Natural and Applied Sciences

Prof. Dr. Süha ORAL
Head of Department, Mechanical Engineering

Prof. Dr. M.Haluk AKSEL
Supervisor, Mechanical Engineering Dept., METU

Examining Committee Members:

Prof. Dr. Kahraman ALBAYRAK
Mechanical Engineering Dept., METU

Prof. Dr. M.Haluk AKSEL
Mechanical Engineering Dept., METU

Asst. Prof. Dr. Cüneyt SERT
Mechanical Engineering Dept., METU

Dr. Tahsin ÇETİNKAYA
Mechanical Engineering Dept., METU

Dr. Mine YUMUŞAK
Roketsan Missiles Industries Inc.

Date: 05.05.2010

I hereby declare that all information in this document has been obtained and presented in accordance with academic rules and ethical conduct. I also declare that, as required by these rules and conduct, I have fully cited and referenced all material and results that are not original to this work.

Name, Last name : Mustafa AKDEMİR

Signature :

ABSTRACT

DEVELOPMENT OF AN AXISYMMETRIC, TURBULENT AND UNSTRUCTURED NAVIER-STOKES SOLVER

AKDEMİR, Mustafa

M. Sc., Department of Mechanical Engineering

Supervisor: Prof. Dr. M.Haluk AKSEL

May 2010, 76 pages

An axisymmetric, Navier-Stokes finite volume flow solver, which uses Harten, Lax and van Leer (HLL) and Harten, Lax and van Leer-Contact (HLLC) upwind flux differencing scheme for spatial and uses Runge-Kutta explicit multi-stage time stepping scheme for temporal discretization on unstructured meshes is developed. Developed solver can solve the compressible axisymmetric flow. The spatial accuracy of the solver can be first or second order accurate. Second order accuracy is achieved by piecewise linear reconstruction. Gradients of flow variables required for piecewise linear reconstruction are calculated by Green-Gauss theorem. Baldwin-Lomax turbulent model is used to compute the turbulent viscosity.

Approximate Riemann solver of HLL and HLLC implemented in solver are validated by solving a cylindrical explosion case. Also the solver's capability of solving unstructured, multi-zone domain is investigated by this problem. First and second order results of solver are compared by solving the flow over a circular

bump. Axisymmetric flow in solid propellant rocket motor is solved in order to validate the axisymmetric feature of solver. Laminar flow over flat plate is solved for viscous terms validation. Turbulent model is studied in the flow over flat plate and flow with mass injection test cases.

Key-words: Navier-Stokes Equations, Second Order Spatial Accuracy, Finite Volume Method, HLL Aproximate Riemann Solver, HLLC Aproximate Riemann Solver, Baldwin-Lomax Turbulence Model

ÖZ

EKSENEL SİMETRİK, TÜRBÜLANSLI VE YAPISAL OLMAYAN BİR NAVIER-STOKES ÇÖZÜCÜSÜ GELİŞTİRİLMESİ

AKDEMİR, Mustafa

Yüksek Lisans, Makina Mühendisliği Bölümü

Tez Yöneticisi: Prof. Dr. M.Haluk AKSEL

Mayıs 2010, 76 sayfa

Zamandan bağımsız, durağan çözümlerinin yapılabilmesi için, düzensiz ve hibrit çözüm ağını uzayda HLL ve HLLC yön hassas (upwind) akı ayırımına dayalı yöntemini, zamanda ise explicit Runge-Kutta çok kademeli yöntemini kullanarak ayrıştıran, iki boyutlu sonlu hacim Navier-Stokes çözücüsü geliştirilmiştir. Geliştirilen Navier-Stokes çözücüsü sıkıştırılabilir akışlar için eksenel simetrik çözümler verebilmektedir. Çözücü uzayda birinci ve ikinci dereceden doğrulukla çözüm yapabilmektedir. Uzayda ikinci dereceden doğruluk, doğrusal yeniden yapılandırma yöntemiyle elde edilmiştir. Doğrusal yeniden yapılandırma için gerekli olan akış değişkenlerinin türevleri Green-Gauss yöntemi kullanılarak hesaplanmaktadır. Turbulanslı akışlarda viskosite hesaplamak için Baldwin-Lomax turbulans modeli kullanılmıştır.

Sonular daha nce yayınlanmıř sonularla ve analitik sonularla karřılařtırılmıřtır. HLL ve HLLC akı ayrıřtırma yntemleri silindirik patlama problemi zlerek dođrulanmıřtır. Uzayda birinci ve ikinci dereceden zmler kanal iinde akıř zlerek karřılařtırılmıřtır. Katı yakıtlı roket motoru i akıřı zlerek zcnn eksele simetrik zelliđi test edilmiřtir. Laminar akıř zmlenme yeteneđi dz plaka zerinde akıř zlerek dođrulanmıřtır. Tubulans modelini dođrulamak iin dz plaka zerinde akıř ve ktle enjeksiyonlu akıř problemleri zlmřtir.

Anahtar Kelime: Navier-Stokes Denklemleri, Uzayda İkinci Derece Doğruluk, Sonlu Hacim Metodu, HLL Akı Ayrıştırma Yöntemi, HLLC Akı Ayrıştırma Yöntemi, Baldwin-Lomax Türbulans Modeli.

ACKNOWLEDGEMENTS

I would like to express my deepest thanks and gratitude to Prof. Dr. Haluk AKSEL for his supervision, encouragement, understanding and constant guidance.

I would like to thank to Bora KALPAKLI for advises on the mathematical work and physics of the test cases.

I would like to use opportunity to thank my colleagues, with whom I had many discussions in the course of this work.

I would like to thank to ROKETSAN for partially supporting this study.

My gratitude is endless for my family whom this thesis is devoted to.

TABLE OF CONTENTS

ABSTRACT	IV
ÖZ	VI
ACKNOWLEDGEMENTS	VIII
TABLE OF CONTENTS	IX
LIST OF FIGURES	XI
LIST OF SYMBOLS	XV
CHAPTERS	1
1. INTRODUCTION	1
1.1. Present Study	6
2. GOVERNING EQUATIONS	8
2.1. Navier-Stokes Equations	8
2.2. Turbulence Model	11
3. NUMERICAL METHODS	14
3.1. Flux Difference Splitting Method	14
3.1.1. Riemann Problem	15
3.1.2. Godunov Approach.....	20
3.1.3. HLL Approximate Riemann Solver	24
3.1.4. HLLC Approximate Riemann Solver	26

3.2.	Evaluation of Viscous Flux	29
3.3.	Coordinate Transformation.....	29
3.4.	Calculation of Time Steps	30
3.5.	Explicit Time Stepping.....	31
3.6.	Data Reconstruction for High Order Accuracy	32
3.6.1.	Limiters.....	32
3.7.	Boundary Conditions.....	34
3.7.1.	Inviscid Wall Boundary Condition.....	34
3.7.2.	Viscous Wall Boundary Condition.....	34
3.7.3.	Far Field Boundary Condition.....	35
3.7.4.	Mass Flow Inlet Boundary Condition.....	37
3.7.5.	Pressure Outlet Boundary Condition.....	38
3.7.6.	Axisymmetric Boundary Condition	39
4.	TEST CASES AND RESULTS	41
4.1.	Cylindrical Explosion.....	42
4.2.	Flow over a Circular Bump	47
4.3.	Inviscid Axisymmetric Flow in SPRM	51
4.4.	Laminar Flow over a Flat Plate.....	54
4.5.	Turbulent Flow over a Flat Plate.....	57
4.6.	Turbulent Flow with Mass Injection	62
5.	CONCLUSION.....	71
	REFERENCES.....	73

LIST OF FIGURES

Figure 3.1 Schematic view of shock tube.....	15
Figure 3.2 Structure of solution of the two-dimensional split Riemann problem..	16
Figure 3.3 Possible wave patterns in the solution of the Riemann problem.....	17
Figure 3.4 Piecewise constant distribution of U variable at time n	20
Figure 3.5 Control volume for solution structure of Riemann problem.....	21
Figure 3.6 Structure of the solution of the HLL approximate Riemann solver	24
Figure 3.7 Structure of the solution of the HLLC approximate Riemann solver...	26
Figure 4.1 Unstructured quadrilateral mesh for the cylindrical explosion	43
Figure 4.2 Unstructured triangular and quadrilateral mesh for the cylindrical explosion.....	44
Figure 4.3 Pressure distribution at $t=0.25$ s. for the quadrilateral mesh.....	44
Figure 4.4 Distribution of the axial velocity at $t=0.25$ s. for the quadrilateral mesh.....	45
Figure 4.5 Density distribution at $t=0.25$ s.....	45
Figure 4.6 Pressure distribution at $t=0.25$ s. for the hybrid grid	46
Figure 4.7 Distribution of the axial velocity at $t=0.25$ s. for the hybrid grid.....	46
Figure 4.8 Density distribution at $t=0.25$ s. for the hybrid grid	47
Figure 4.9 Grid for flow over circular bump problem.....	48

Figure 4.10 Distribution of Mach number for first order spatial accuracy	49
Figure 4.11 Mach number contour for first order spatial accuracy with HLL method.....	49
Figure 4.12 Mach number contour for first order spatial accuracy with HLLC method.....	50
Figure 4.13 Distribution of Mach number for second order spatial accuracy	50
Figure 4.14 Mach number contour for second order spatial accuracy with HLL method.....	51
Figure 4.15 Mach number contour for second order spatial accuracy with HLLC method.....	51
Figure 4.16 Mesh used for SPRM	52
Figure 4.17 Mach number along the symmetry axis	52
Figure 4.18 Pressure (atm) along the symmetry axis	53
Figure 4.19 Mach contour of SPRM.....	53
Figure 4.20 Grid used for the laminar flow over a flat plate.....	54
Figure 4.21 Comparison of tangential velocity profile with Blasius solution at $x/c=0.5$	55
Figure 4.22 Comparison of normal velocity profile with Blasius solution at $x/c=0.5$	56
Figure 4.23 Comparison of skin friction coefficient with the analytical solution at $x/c=0.5$	57
Figure 4.24 Hybrid mesh consisting of triangular cells and boundary layer	58
Figure 4.25 Structured grid consisting of quadrilateral cells and boundary layer ..	59

Figure 4.26 Comparison of tangential velocity profile with Prandtl's turbulent solution.....	60
Figure 4.27 Turbulent similarity profiles for different location.....	60
Figure 4.28 Comparison of skin friction coefficient with the analytical solution..	61
Figure 4.29 Comparison of skin friction coefficient for hybrid and structured grid	61
Figure 4.30 VECLA setup	62
Figure 4.31 Grid used for the turbulent flow with mass injection	63
Figure 4.32 Axial velocity profiles at $x = 0.570$ m.....	64
Figure 4.33 Axial velocity profiles at $x = 0.500$ m.....	64
Figure 4.34 Axial velocity profiles at $x = 0.450$ m.....	65
Figure 4.35 Axial velocity profiles at $x = 0.400$ m.....	65
Figure 4.36 Axial velocity profiles at $x = 0.350$ m.....	66
Figure 4.37 Axial velocity profiles at $x = 0.220$ m.....	66
Figure 4.38 Axial velocity profiles at $x = 0.120$ m.....	67
Figure 4.39 Analitical and computed axial velocity profiles at $x = 0.500$ m for laminar and turbulent flows.	68
Figure 4.40 Analitical and computed axial velocity profiles at $x = 0.450$ m for laminar and turbulent flows.	68
Figure 4.41 Analitical and computed axial velocity profiles at $x = 0.400$ m for laminar and turbulent flows.	69
Figure 4.42 Analitical and computed axial velocity profiles at $x = 0.350$ m for laminar and turbulent flows.	69

Figure 4.43 Analytical and computed axial velocity profiles at $x = 0.220$ m for laminar and turbulent flows. 70

Figure 4.44 Analytical and computed axial velocity profiles at $x = 0.120$ m for laminar and turbulent flows. 70

LIST OF SYMBOLS

A	projection of control volume
a	speed of sound
C_f	local friction coefficient
E	total internal energy per unit volume
F	x-component of flux vector
G	y-component of flux vector
\vec{i}	unit normal vector in x-direction
\vec{j}	unit normal vector in y-direction
L	length
\dot{m}	mass flux
M	Mach number
\vec{n}	normal vector
Pr	Prandtl number
p	pressure
Re	Reynolds number
R	gas constant, residual
r	radial coordinate
S	wave speed, source term
t	time
T	temperature
U	vector of conservative variables
u	x-component of velocity vector

q	heat flux
V	area of the cell
v	y-component of velocity vector
x,y	Cartesian space coordinates

Other Symbols:

ρ	density
γ	specific heat ratio
∂	partial derivative operator
τ	shear stress
μ	viscosity
κ	thermal conductivity, limiter function parameter
η	Blasius similarity variable
α	Runge-Kutta method coefficients

Superscripts:

n	quantity at discrete time level n
\wedge	values of vector normal to the face

Subscripts:

c	values of geometric variables for the axisymmetry
d	values of domain
f	values of face
G	values of ghost cell
i	cell number
L	value at the left hand side of a face, laminar values
R	value at the right hand side of a face

<i>inj</i>	injection property
<i>n</i>	normal component
<i>0</i>	stagnation state
<i>max</i>	maksimum value
<i>min</i>	minimum value
<i>x</i>	x component
<i>T</i>	turbulent values
<i>y</i>	y component
<i>v</i>	viscous terms, Venkattakrishnan
∞	freestream value
*	values for the region between the waves

CHAPTER 1

INTRODUCTION

The use of computational methods in fluid dynamics applications is expanding throughout industry, academia, defense and research community. Advances in computers' skills such as speed, capacity, etc. are making the Computational Fluid Dynamics (CFD) to become an unchangeable part of life. Especially in design process having an interaction with a flow, CFD is increasingly being used.

There are four main methods using for computational engineering. Those are

- Finite Difference Method (FDM)
- Finite Element Method (FEM)
- Spectral Method
- Finite Volume Method (FVM)

Finite Volume Method is one of the popular methods used in CFD. In FVM, physical space of flow is divided into small control volumes. In FVM method, fluxes are evaluated at the faces of control volume. Integral form of conservation laws is used in FVM, so the mass, momentums and energy are conserved over each control volumes. Surface integral of fluxes is assumed to be equal to the sum of the fluxes crossing the faces of these control volumes. There are several spatial discretisation methods used in approximation

of convective and viscous fluxes separately. For convective fluxes, these methods can be classified as central methods, upwind methods. Temporal discretisation methods can also be classified into two groups. Those are Explicit Time Stepping Algorithms and Implicit Time Stepping Algorithms. In Implicit Time Stepping Algorithms, there is a high convergence rate but it requires large amount of memory. Also implementation of implicit time stepping is more complicated than the explicit one. In Explicit Time Stepping Algorithms, convergence rate is lower than the implicit one. In the case required coarse mesh, explicit time stepping may be efficient. However, solution of Navier-Stokes equations requires fine meshes especially within the boundary layer.

It is necessary to solve the Navier-Stokes equations in order to analyse the flow field in detail. Also dependence of viscosity and thermal conductivity to a thermodynamic property has to be achieved in order to achieve an accurate simulation of flow. For laminar flows, the viscosity and thermal conductivity can be defined as a function of temperature.

The main problem in numerical solutions of Navier-Stokes equations is the existence of the many different length scales and time scales, due to the different natures of each physical phenomena. Typical length scales for a boundary layer thickness, the viscous thickness of a shock wave and the turbulent eddy are in the order of $\frac{1}{\sqrt{Re}}$, $\frac{1}{Re}$ and $\frac{1}{Re^2}$ respectively. These scalings differ by orders of magnitude in any flow. Since all of them cannot be handled, the unresolved scalings must be modeled, either by physical closures (like turbulence) or by numerical means (like shock capturing). Inside the viscous layers like boundary layers and wakes, order of magnitude of convective and viscous terms are balanced. Thus the solution becomes continuous but shows large gradients in variables. This fact can lead to severe problems of accuracy of the numerical method if these layers are not resolved sufficiently well [1].

The main characteristic of the compressible flows is the occurrence of discontinuities in flow variables and also in fluid properties. The occurrence of discontinuities and their

interactions may have strong effects on flow characteristics. For the flow field with the significant discontinuities, flow direction information is required to solve the problem accurately. Upwind schemes are developed which take the direction of the flow into consideration. Upwind schemes are the major spatial discretization methods used in CFD [2]. There are two basic ways of using the upwind schemes: flux-vector splitting (FVS) methods and flux-difference splitting (FDS) methods.

In flux-vector splitting, the flux vector is split into two parts based on the information coming from upwind and downwind of the cell face [3]. The flux terms are split according to the sign of characteristic variables into a convective and a pressure part [4]. Van Leer's method splits the fluxes according to the sign of characteristic variables [5], while Advection Upstream Splitting Method (AUSM) splits the fluxes into convective and pressure part [6].

In flux-difference splitting method, a local Riemann problem is solved at each face of cells using left and right state of the corresponding face. The flow variables are taken as constant over the left and right states of the cell face. Flux-difference splitting method was introduced by Godunov [7], who solved the local Riemann problem exactly. He proposed that the non-linear superposition of the Riemann problems which lead to a general initial value problem. Thus the exact solution of Riemann problem gives almost the exact results of the initial value problem. Since the exact solution of Riemann problem is computationally expensive, some approximate Riemann solvers have been developed by Roe [8], Osher and Solomon [9], Toro [10] and Harten [11].

In order to use the flux-difference splitting method with the approximate Riemann solver, Harten, Lax and van Leer [12] introduced an efficient and robust approach called Harten, Lax and van Leer (HLL) approximate Riemann solver method [10]. Davis [13] and Einfeldt [14] derived the methods for computing the wave speeds required by HLL method. Based on HLL approximate Riemann solver, the high-resolution TVD schemes have been introduced Mingham and Causonb [15] and Hu [16]. By using the HLL scheme as a basis for developing second-order TVD schemes, shallow water flows were

solved. ADER-HLL method which is a higher order version of HLL approximate Riemann solver was introduced by Titarev and Toro. One disadvantage of HLL method is the assumption of two-wave structure. For Euler equations, this assumption is not true. Some physical features such as entropy waves, slip surfaces, material interfaces, vertical flows, shear layers and contact discontinuities may be resolved inaccurately by using HLL approximate Riemann solver. Wackers and Koren [17] adopted the HLL approximate Riemann solver to two-fluid flow. The source term in the flow equations is incorporated into the HLL solver of the Riemann by Wackers and Koren.

Toro, Spruce and Speares [18] presented a new method called Harten, Lax and van Leer–Contact (HLLC) which overcome the two-wave structure disadvantage of HLL method by considering the contact wave speeds. HLLC is useful and efficient approximate Riemann solver for practical applications. Two dimensional multi phase flow was solved by Toro by using HLLC approximate Riemann solver [10]. Shallow water equations were solved with the HLLC approximate Riemann solver by Toro in 2001 [10]. A new high order accurate method named ADER-HLLC was presented by Titarev and Toro. HLLC method was implemented to an implicit solver by Batten, Goldberg and Leschziner [19] and has been used to solve the turbulent flows.

In the Navier-Stokes equations, the coefficients of viscosity and thermal conductivity are represented as functions of temperature for laminar flow. Hence, Navier-Stokes equations and constitutive relations are sufficient to handle the laminar cases. Looking at the turbulent cases, the situation is more complex to handle where turbulence is characterized by random fluctuation of the flow properties. Since time history is not of a great interest one would integrate the flow properties over a period of time to extract time-averages, which is an adopted technique by engineers. For turbulent flows, turbulent features of flows are modeled since the length scale of turbulent eddy is so small.

The turbulence models had been classified under four main categories. They are:

- algebraic (zero-equation) models

- one-equation models
- two-equation models and
- second-order closure models

Many turbulence models, however, are cumbersome to implement and require a lot of computer time to run, since they add a number of differential equations to be solved to model a flow. The algebraic turbulence models are the simplest of all turbulence models. After Prandtl, the first contribution was due to Van Driest who proposed that the mixing length must be multiplied by a viscous damping correlation. These models use the Boussinesq eddy-viscosity approximation to compute the Reynolds stress tensor. Cebeci-Smith and Baldwin-Lomax are the most important ones of the algebraic turbulence models. The Baldwin-Lomax turbulence model is superior in separated flows, especially for flows with shock waves. The algebraic models are incomplete models of turbulence, because the eddy viscosity as well as the mixing length depends on the type of flow that is being considered [20].

The Baldwin-Lomax turbulence model is a popular model. It is an algebraic, eddy viscosity model. The Baldwin-Lomax model is used in many CFD codes because it is quick and easy to implement. And also Baldwin-Lomax model is suitable for separated or attached flows. Sakowski, Roach and Wall implemented the Baldwin-Lomax turbulence model for both steady and unsteady compressible flows in engine inlets. They did some modifications in order to apply this turbulence model to engine inlet flows.

Because of easiness of implementation and having capability of solving the attached and separated flow Baldwin-Lomax turbulence model is selected to implement the developed code.

1.1. Present Study

The purpose of this study is to develop a two-dimensional flow solver, which can be used for the analysis of internal flows in solid propellant rocket motors in order to analyze its performance.

Flow solver is capable of solving Navier-Stokes equations in two dimensions for steady state problems. It uses the finite volume method, with upwind flux calculation of HLL and HLLC. Moreover, the solver can operate on structured and unstructured grids. For the integration of governing equations in time, solver uses explicit methods. Accuracy of spatial discretization can be selected to be first and second order. Baldwin-Lomax turbulence model is used.

The developed solver, which is described in this thesis, is validated with the results of previously validated performance prediction codes.

The governing equations of flow and the equation of turbulence model used in thesis are explained in Chapter 2.

Chapter 3 discusses the spatial and temporal discretization methods used in this thesis. The details of spatial discretization are presented for convective and viscous fluxes separately. Convective fluxes are calculated by using the HLL and HLLC approximate Riemann solver. Also, how second order of accuracy of convective flux calculation is introduced. Also, the explicit Multi-Stage Runge Kutta Method time discretization method is explained. Coordinate transformation and calculation of time steps is explained in Chapter 3. This chapter concludes with the description of boundary conditions used in the solver developed.

Test cases and the results of the solver are presented in Chapter 4. Approximate Riemann solver of HLL and HLLC is validated by solving a cylindrical explosion case. Also the solver's capability of solving unstructured, multi-zone domain is investigated by this

problem. Assessment of higher order accuracy of the solver is validated by solving the flow over a circular bump. Axisymmetric flow in solid propellant rocket motor is solved in order to validate the axisymmetric property of the solver. Laminar flow solving capability is tested by solving the flow over a flat plate. Also turbulent flow solving capability is tested by using this case and the flow with mass injection case.

CHAPTER 2

GOVERNING EQUATIONS

2.1. Navier-Stokes Equations

The flow of a viscous, heat conducting, compressible gas without body force and heat generation can be modeled by the Navier-Stokes equations. In two dimensions, the conservative formulation of the Navier-Stokes equations can be written in differential form in terms of conservative variables as:

$$\frac{\partial U}{\partial t} + \frac{\partial(F - F_v)}{\partial x} + \frac{\partial(G - G_v)}{\partial y} = 0 \quad (2.1)$$

where

$$U = \begin{bmatrix} \rho \\ \rho u \\ \rho v \\ E \end{bmatrix} \quad (2.2)$$

where t is the time, ρ is the density, E is the total internal energy per unit volume, u and v are the velocity components in x and y directions, respectively.

$$F = \begin{bmatrix} \rho u \\ \rho u u + p \\ \rho u v \\ u(E + p) \end{bmatrix} \quad (2.3)$$

where p is the pressure.

$$G = \begin{bmatrix} \rho v \\ \rho v u \\ \rho v v + p \\ v(E + p) \end{bmatrix} \quad (2.4)$$

$$F_v = \begin{bmatrix} 0 \\ \tau_{xx} \\ \tau_{xy} \\ u\tau_{xx} + v\tau_{xy} + q_x \end{bmatrix} \quad (2.5)$$

$$G_v = \begin{bmatrix} 0 \\ \tau_{yx} \\ \tau_{yy} \\ u\tau_{yx} + v\tau_{yy} + q_y \end{bmatrix} \quad (2.6)$$

The shear stress components are expressed as;

$$\tau_{xx} = \mu \left(\frac{4}{3} \frac{\partial u}{\partial x} - \frac{2}{3} \frac{\partial v}{\partial y} \right) \quad (2.7)$$

$$\tau_{yy} = \mu \left(\frac{4}{3} \frac{\partial v}{\partial y} - \frac{2}{3} \frac{\partial u}{\partial x} \right) \quad (2.8)$$

$$\tau_{xy} = \mu \left(\frac{\partial u}{\partial y} + \frac{\partial v}{\partial x} \right) \quad (2.9)$$

$$\tau_{yx} = \tau_{xy} \quad (2.10)$$

where μ is the total effective viscosity coefficient. Total effective viscosity is defined by using the eddy-viscosity concept as follows [21]

$$\mu = \mu_{lam} + \mu_{turb} \quad (2.11)$$

where μ_{lam} and μ_{turb} are the laminar and turbulent viscosities, respectively. The Sutherland formula [21] is used for the laminar viscosity, μ_{lam} ,

$$\mu_{lam} = 1.45 \times 10^{-6} \frac{T^{\frac{2}{3}}}{T + 110} \quad (2.12)$$

Evaluation of the turbulent viscosity, μ_{turb} , is explained in detail in next section.

The components of heat flux are expressed as follows;

$$q_x = -\kappa \frac{\partial T}{\partial x} \quad (2.13)$$

$$q_y = -\kappa \frac{\partial T}{\partial y} \quad (2.14)$$

where T and κ are the temperature and thermal conductivity, respectively.

To close the system of equations, the equation of state for an ideal gas is used

$$E = \rho e + \frac{1}{2} \rho (u^2 + v^2) \quad (2.15)$$

$$e = \frac{p}{(\gamma-1)\rho} \quad (2.16)$$

where e and γ is the specific internal energy and the specific heat ratio, respectively.

2.2. Turbulence Model

Baldwin-Lomax turbulence model is employed to calculate the turbulent viscosity. This model defines the turbulent viscosity as follows [22]

$$\mu_{turb} = \begin{cases} (\mu_{turb})_{inner} & \text{if } Y \leq Y_{crossover} \\ (\mu_{turb})_{outer} & \text{if } Y \geq Y_{crossover} \end{cases} \quad (2.17)$$

In the above equation, Y is the normal distance from the wall and $Y_{crossover}$ is the value of Y at which values of inner and outer formulas are equal.

Inner layer turbulent viscosity based on the Prandtl mixing length theory is

$$(\mu_{turb})_{inner} = \rho l_{inner}^2 |\bar{\omega}| \quad (2.18)$$

where l_{inner} is the mixing length and defined as follows

$$l_{inner} = 0.4Y \left(1 - e^{-\frac{Y^+}{26}}\right) \quad (2.19)$$

$\bar{\omega}$ is the vorticity and given as follows

$$\bar{\omega} = \left(\frac{\partial v}{\partial x} - \frac{\partial u}{\partial y} \right) \bar{k} \quad (2.20)$$

Y^+ is the non-dimensional wall distance and defined as

$$Y^+ = \left(\frac{\rho u_\tau}{\mu_{lam}} \right)_{wall} Y \quad (2.21)$$

where the friction velocity, u_τ , is given as

$$u_\tau = \sqrt{\frac{\tau_{wall}}{\rho_{wall}}} \quad (2.22)$$

The turbulent viscosity in the outer layer is given as

$$(\mu_{turb})_{outer} = 0.0168 C_{cp} \rho F_{wake} F_{kleb}(Y) \quad (2.23)$$

where the F_{wake} is given as

$$F_{wake} = \min \left\{ \begin{array}{l} Y_{max} F_{max} \\ C_{WK} Y_{max} \frac{V_{diff}^2}{F_{max}} \end{array} \right. \quad (2.24)$$

$Y_{max} F_{max}$ term in above equation is valid for attached wall boundary layers while the

$C_{WK} Y_{max} \frac{V_{diff}^2}{F_{max}}$ term is valid for separated and attached wall boundary layers and wakes

where $C_{cp} = 1.6$ and $C_{WK} = 0.25$ [22]. Y_{max} is the Y value at which the F is maximum.

Following equation is used to calculate the velocity difference, V_{diff} .

$$V_{diff} = (V)_{\max} - (V)_{\min} \quad (2.25)$$

where $(V)_{\max}$ is the magnitude of velocity corresponding to F_{\max} as $Y_{\max} \cdot (V)_{\min}$ is the minimum velocity of the profile [22]. The vorticity moment F is calculated as follows

$$F(Y) = \begin{cases} Y|\bar{\omega}|(1 - e^{-\frac{Y^+}{26}}) \\ Y|\bar{\omega}| \end{cases} \quad (2.26)$$

In the above equation, $Y|\bar{\omega}|$ term is applied to wakes while the other one is applied to the wall boundary layer.

For the evaluation of outer layer turbulent viscosity, the Klebanoff intermittency factor is used so the outer turbulent viscosity is vanish as Y goes to infinity. This factor is given as

$$F_{Kleb}(Y) = \frac{1}{1 + 5.5\left(\frac{C_{Kleb} \cdot Y}{Y_{\max}}\right)^6} \quad (2.27)$$

CHAPTER 3

NUMERICAL METHODS

Basic parts of numerical methods being used for analyzing a flow are the spacial discretisation and temporal discretisation. There are so many methods for special and temporal discretisation. This chapter mainly introduces these methods. Firstly, spacial discretisation method of flux differencing method for convective flux will be presented. Evaluation of viscous fluxes will be introduced next. Developed code can analyze a flow on unstructured grid, so the coordinate transformation is needed. This subject will be discussed after the viscous flux. After the subjects of spatial discretisation, temporal discretisation subjects, calculation of time steps and explicit time stepping, will be presented. This will be followed by the description of data reconstruction for higher order accuracy and the limiter. Finally boundary conditions will be defined.

3.1. Flux Difference Splitting Method

Flux difference splitting method evaluates the fluxes at the faces of the control volume from the left and the right sides conditions by solving the Riemann shock tube problem. The idea of flux difference splitting method was first introduced by Godunov [7]. Flux difference splitting method considers not only direction of waves but also the waves themselves. The solution of the Riemann problem may employ exact or approximate solvers. Exact solution of Riemann shock tube problem is required so much

computational effort. So many approximate Riemann solvers were presented in literature [4].

3.1.1. Riemann Problem

Riemann problem is, simply, the initial value problem of hyperbolic systems. This problem is important because the exact time-dependent solution is known. This known solution can be compared with the solution computed by using any numerical method in order to validate the used method.

The Riemann problem or the initial value problem for 1-D Euler equations can be formulated as follow:

$$\frac{\partial U}{\partial t} + \frac{\partial F}{\partial x} = 0 \quad (3.1)$$

with the initial conditions

$$U(x, t_0) = \begin{cases} U_L & \text{if } x < x_0 \\ U_R & \text{if } x > x_0 \end{cases} \quad (3.2)$$

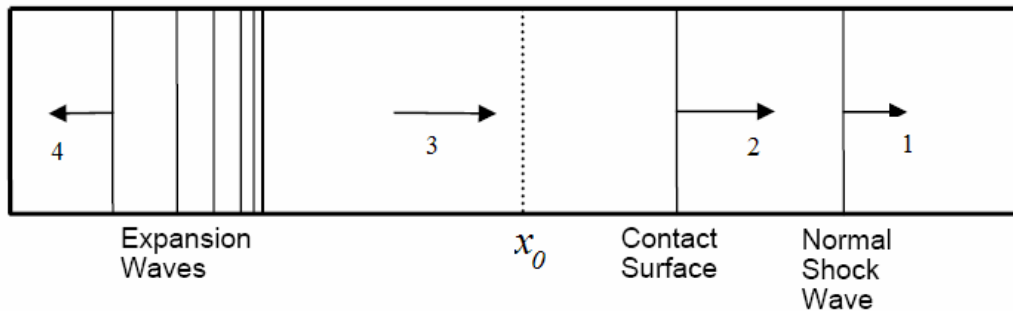


Figure 3.1 Schematic view of shock tube

Practically Riemann problem is experienced the flow through a shock tube flow as shown in Figure 3.1. The gas on two side of the tube is separated by a diaphragm at the point x_0 at the time t_0 . If the viscous forces are neglected and the tube is assumed to be infinitely long, the exact solution of the Euler equations can be obtained.

In the shock tube, there are two regions separated from each other by the diaphragm. Initially the left and the right sides of diaphragm contain same gas at different states called U_L and U_R .

After the sudden rupture of the diaphragm, expansion waves move to the high-pressure side in order to decrease the pressure; and a normal shock wave moves to the low-pressure side to increase the pressure. A contact surface is formed between the normal shock wave and the tail of the expansion waves [10].

For two dimensional Euler equations, there is one additional characteristic field associated with the eigen value having the value \hat{u} . This is a shear wave across which the tangential velocity component \hat{v} changes discontinuously. In the star region, between the right and left waves, pressure p and normal velocity \hat{u} are constant. Structure of the solution of the local Riemann problem can be seen in Figure 3.2. All variables, superscripted with (^), represent the value according the facial coordinate.

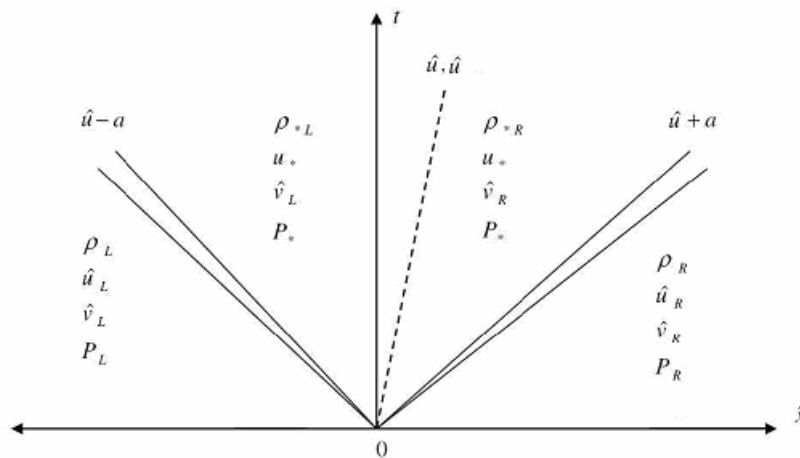


Figure 3.2 Structure of solution of the two-dimensional split Riemann problem

There are four possible wave patterns in the solution of Riemann problem. Those are can be listed as follows and shown in Figure 3.3.

- Left rarefaction, contact and right shock (a)
- Left rarefaction, contact and right rarefaction (b)
- Left shock, contact and right shock (c)
- Left shock, contact and right rarefaction (d)

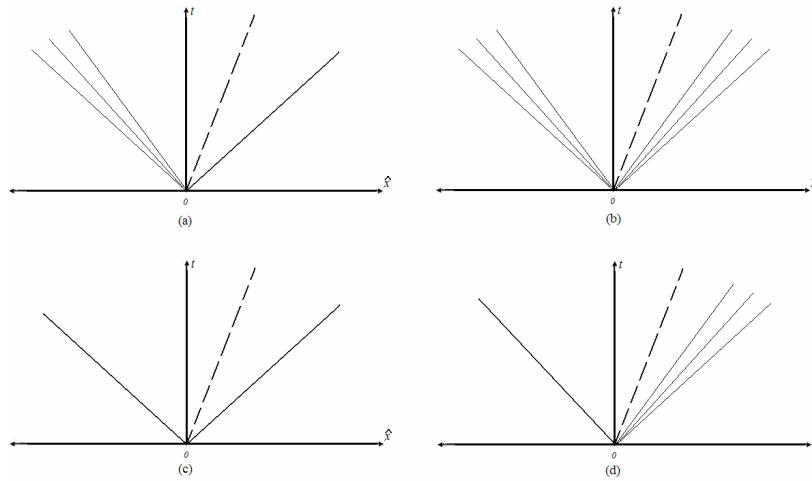


Figure 3.3 Possible wave patterns in the solution of the Riemann problem

As can be seen in Figure 3.2, in star region between the left and right wave, values of primitive variables are as follows:

$$\begin{aligned}
 p_{*R} &= p_{*L} = p_* \\
 \hat{u}_{*R} &= \hat{u}_{*L} = \hat{u}_* \\
 \hat{v}_{*R} &= \hat{v}_R \\
 \hat{v}_{*L} &= \hat{v}_L
 \end{aligned} \tag{3.3}$$

Knowing the values of primitive variables in left and right regions, p_* , \hat{u}_* , ρ_{*L} and ρ_{*R} are variables to be evaluated.

p_* can be evaluated exactly by solving for the root of the following equation [10].

$$f_L(p_*, W_L) + f_R(p_*, W_R) + \hat{u}_R - \hat{u}_L = 0 \quad (3.4)$$

where function f_L and f_R represents the relations between the left star region and the left region and the right star region and the right region respectively and given as

$$f_L(p_*, W_L) = \begin{cases} (p_* - p_L) \left[\frac{2/(\gamma+1)\rho_L}{p_* + \frac{\gamma-1}{\gamma+1}p_L} \right]^{1/2} & , p_* > p_L \\ \frac{2a_L}{\gamma-1} \left[\left(\frac{p_*}{p_L} \right)^{\frac{\gamma-1}{2\gamma}} - 1 \right] & , p_* \leq p_L \end{cases} \quad (3.5)$$

$$f_R(p_*, W_R) = \begin{cases} (p_* - p_R) \left[\frac{2/(\gamma+1)\rho_R}{p_* + \frac{\gamma-1}{\gamma+1}p_R} \right]^{1/2} & , p_* > p_R \\ \frac{2a_R}{\gamma-1} \left[\left(\frac{p_*}{p_R} \right)^{\frac{\gamma-1}{2\gamma}} - 1 \right] & , p_* \leq p_R \end{cases} \quad (3.6)$$

The solution for \hat{u}_* is given as [1]

$$\hat{u}_* = \frac{1}{2}(\hat{u}_R + \hat{u}_L) + \frac{1}{2}[f_R(p_*) + f_L(p_*)] \quad (3.7)$$

After evaluation of the \hat{u}_* and p_* , other unknown variables ρ_{*L} and ρ_{*R} can be evaluated by using the following relations between the density ratio and the pressure ratio across the shock waves.

$$\rho_{*L} = \rho_L \left[\frac{\frac{p_*}{p_L} + \frac{\gamma-1}{\gamma+1}}{\frac{\gamma-1}{\gamma+1} \frac{p_*}{p_L} + 1} \right] \quad (3.8)$$

$$\rho_{*R} = \rho_R \left[\frac{\frac{p_*}{p_R} + \frac{\gamma-1}{\gamma+1}}{\frac{\gamma-1}{\gamma+1} \frac{p_*}{p_R} + 1} \right] \quad (3.9)$$

If the types of waves are the rarefaction following relations are used for calculation of ρ_{*L} and ρ_{*R} .

$$\rho_{*L} = \rho_L \left(\frac{p_*}{p_L} \right)^{\frac{1}{\gamma}} \quad (3.10)$$

$$\rho_{*R} = \rho_R \left(\frac{p_*}{p_R} \right)^{\frac{1}{\gamma}} \quad (3.11)$$

Wave speeds S_R , S_L and S_* for Riemann problem can be calculated as follows:

$$S_R = \hat{u}_R + a_R \sqrt{\frac{\gamma+1}{2\gamma} \frac{p_*}{p_R} + \frac{\gamma+1}{2\gamma}} \quad (3.12)$$

$$S_L = \hat{u}_L - a_L \sqrt{\frac{\gamma+1}{2\gamma} \frac{p_*}{p_R} + \frac{\gamma+1}{2\gamma}} \quad (3.13)$$

$$S_* = \hat{u}_* \quad (3.14)$$

The inter-cell flux at a face f for the exact Riemann solver is given as follows: [10]

$$F_f^{exact} = \begin{cases} F_L & , 0 \leq S_L \\ F_{*L} & , S_L \leq 0 \leq S_* \\ F_{*R} & , S_* \leq 0 \leq S_R \\ F_R & , 0 \leq S_R \end{cases} \quad (3.15)$$

Detailed explanation of exact solution of Riemann problem can be seen in reference [10].

3.1.2. Godunov Approach

Finite difference formulations assume that the functions are sufficiently smooth, continuous and continuously differentiable at the order of accuracy. This assumption is not valid for flows consisting discontinuities like shock waves. Godunov introduced a finite volume method called flux difference splitting scheme to overcome the problem encountered while discontinuities occur in flow. Basis of Godunov approach is the handling the flow by evaluating the fluxes using the solution of Riemann problem [10].

The Godunov approach considers the solution to be constant over a cell at a fixed time, t , as shown in Figure 3.4. The cell interfaces are assumed to be similar to the diaphragm in the shock tube. The flow field variables at the next time step are evaluated by assuming that there is a local Riemann problem [23].

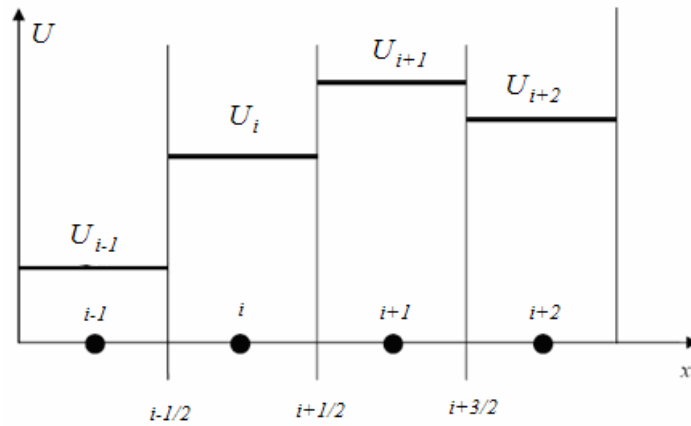


Figure 3.4 Piecewise constant distribution of U variable at time n .

Exact solution of Riemann problem is computationally expensive, so approximate Riemann solvers, HLL and HLLC are used. Before introducing the approximate Riemann solvers, integral relations of solution structure is discussed.

In Figure 3.5, control volume is given as $[x_L, x_R] \times [0, T]$. Integral form of the conservation laws as in follows:

$$\int_{x_L}^{x_R} \hat{U}(x, T) dx = \int_{x_L}^{x_R} \hat{U}(x, 0) dx + \int_0^T F(\hat{U}(x_L, t)) dt - \int_0^T F(\hat{U}(x_R, t)) dt \quad (3.16)$$

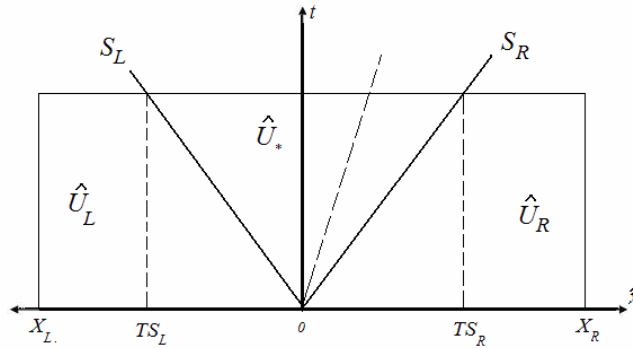


Figure 3.5 Control volume for solution structure of Riemann problem

Right hand side above equation can be written as follows:

$$\int_{x_L}^{x_R} \hat{U}(x, T) dx = x_R \hat{U}_R - x_L \hat{U}_L + TF_L(\hat{U}_L) - TF_R(\hat{U}_R) \quad (3.17)$$

Left hand side of equation in integral form can be split into three integrals as follows:

$$\int_{x_L}^{x_R} \hat{U}(x, T) dx = \int_{x_L}^{TS_L} \hat{U}(x, T) dx + \int_{TS_L}^{TS_R} \hat{U}(x, T) dx + \int_{TS_R}^{x_R} \hat{U}(x, T) dx \quad (3.18)$$

Some parts of above equation can be evaluated as follows:

$$\int_{x_L}^{x_R} \hat{U}(x, T) dx = TS_L \hat{U}_L - x_L \hat{U}_L + \int_{TS_L}^{TS_R} \hat{U}(x, T) dx - TS_R \hat{U}_R + x_R \hat{U}_R \quad (3.19)$$

From Equation 3.4 and Equation 3.6, one can obtain

$$\int_{TS_L}^{TS_R} \hat{U}(x, T) dx = TS_R \hat{U}_R - TS_L \hat{U}_L + TF_L - TF_R \quad (3.20)$$

Integral average of solution, \hat{U}_* , between the waves S_L and S_R can be calculated as follows:

$$\hat{U}_* = \frac{1}{TS_R - TS_L} \int_{TS_L}^{TS_R} \hat{U}(x, T) dx = \frac{TS_R \hat{U}_R - TS_L \hat{U}_L + TF_L - TF_R}{TS_R - TS_L} \quad (3.21)$$

Integral form of conservation laws in control volume $[x_L, 0] \times [0, T]$, the left side of the t axis in Figure 3.5 given as follows:

$$\int_{x_L}^0 \hat{U}(x, T) dx = \int_{x_L}^0 \hat{U}(x, 0) dx + \int_0^T F(\hat{U}(x_L, t)) dt - \int_0^T F(\hat{U}(0, t)) dt \quad (3.22)$$

Right hand side of above equation can be written as

$$\int_{x_L}^0 \hat{U}(x, T) dx = -x_L \hat{U}_L + TF_L - TF_{0L} \quad (3.23)$$

Left hand side of above equation can be split into two integral.

$$\int_{x_L}^{TS_L} \hat{U}(x, T) dx + \int_{TS_L}^0 \hat{U}(x, T) dx = -x_L \hat{U}_L + TF_L - TF_{0L} \quad (3.24)$$

After evaluating the first term of left hand side following equation is obtained.

$$\int_{TS_L}^0 \hat{U}(x, T) dx = -TS_L \hat{U}_L + TF_L - TF_{0L} \quad (3.25)$$

Solving for F_{0L} we find

$$F_{0L} = F_L - S_L U_L - \frac{1}{T} \int_{TS_L}^0 \hat{U}(x, T) dx \quad (3.26)$$

Integral form of conservation laws in control volume $[0, x_R] \times [0, T]$, the right side of the t axis in Figure 3.5 given as follows:

$$\int_0^{x_R} \hat{U}(x, T) dx = \int_0^{x_R} \hat{U}(x, 0) dx + \int_0^T F(\hat{U}(0, t)) dt - \int_0^T F(\hat{U}(x_R, t)) dt \quad (3.27)$$

Right hand side of above equation can be written as

$$\int_{x_L}^0 \hat{U}(x, T) dx = x_R \hat{U}_R + TF_{0R} - TF_R \quad (3.28)$$

Left hand side of above equation can be split into two integral.

$$\int_{TS_R}^{x_R} \hat{U}(x, T) dx + \int_{TS_R}^0 \hat{U}(x, T) dx = x_R \hat{U}_R + TF_{0R} - TF_R \quad (3.29)$$

After evaluating the first term of left hand side following equation is obtained.

$$\int_0^{TS_R} \hat{U}(x, T) dx = TS_R \hat{U}_R + TF_{0R} - TF_R \quad (3.30)$$

Solving for F_{0R} we find

$$F_{0R} = F_R - S_R U_R + \frac{1}{T} \int_0^{TS_R} \hat{U}(x, T) dx \quad (3.31)$$

From Equations 3.20, 3.25 and 3.30 following equality can be obtained

$$F_{0R} = F_{0L} \quad (3.32)$$

3.1.3. HLL Approximate Riemann Solver

The HLL approximate Riemann solver is based on the integral form of the conservation laws and the largest and smallest wave speed in the Riemann problem. The stability and robustness of the HLL solver is closely related to the wave speeds. Main part of this solver is that the structure of solution is assumed to have two waves as indicated in Figure 3.6.

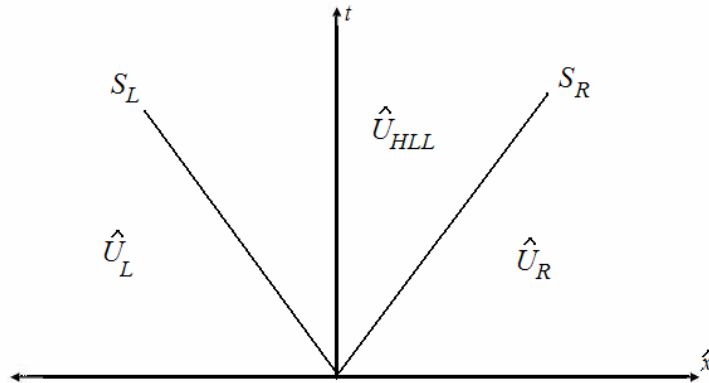


Figure 3.6 Structure of the solution of the HLL approximate Riemann solver

HLL approximate Riemann solver assumes two wave structures so there are three separate regions. If the interface of two corresponding cells is in the left region of S_L inter-cell flux is determined as F_L . The inter-cell flux determined as F_R if the interface is in the right side of the S_R . If the interface is in the region between the two waves, inter-cell flux is F_{OL} or F_{OR} which are equal. F_{OR} can be obtained as follow by substitution \hat{U}_* from Equation 3.8 into the Equation 3.18.

$$F_{OR} = \frac{S_R F_L - S_L F_R + S_R S_L (\hat{U}_R - \hat{U}_L)}{S_R - S_L} \quad (3.33)$$

The inter-cell flux at a face f for the HLL approximate Riemann solver is given as follows [10]

$$F_f^{HLL} = \begin{cases} F_L & , 0 \leq S_L \\ \frac{S_R F_L - S_L F_R + S_R S_L (\hat{U}_R - \hat{U}_L)}{S_R - S_L} & , S_L \leq 0 \leq S_R \\ F_R & , 0 \geq S_R \end{cases} \quad (3.34)$$

The right and left wave speeds, S_L and S_R , can be estimated by using two different methods. Simple direct estimation is given by Davis [13] as

$$S_L = \min(\hat{u}_R - a_R, \hat{u}_L - a_L) \quad (3.35)$$

$$S_R = \max(\hat{u}_R + a_R, \hat{u}_L + a_L) \quad (3.36)$$

An estimation leading effective and robust schemes is proposed by Einfeldt [14] as

$$S_L = \hat{u} - \hat{d} \quad S_R = \hat{u} + \hat{d} \quad (3.37)$$

where

$$\hat{d} = \left(\frac{\sqrt{\rho_L} \cdot a_L^2 + \sqrt{\rho_R} \cdot a_R^2}{\sqrt{\rho_L} + \sqrt{\rho_R}} + \frac{1}{2} \frac{\sqrt{\rho_L} \sqrt{\rho_R}}{(\sqrt{\rho_L} + \sqrt{\rho_R})^2} \right)^{1/2} \quad (3.38)$$

\hat{u} is the Roe averaged speed normal to the face and can be given by

$$\hat{u} = \frac{\sqrt{\rho_L} \hat{u}_L + \sqrt{\rho_R} \hat{u}_R}{\sqrt{\rho_L} + \sqrt{\rho_R}} \quad (3.39)$$

3.1.4. HLLC Approximate Riemann Solver

The HLLC approximate Riemann solver was introduced by Toro [10]. Some physical features can be resolved inaccurately by using HLL solver as a result of the assumed two-wave structure. HLLC Riemann solver can overcome this problem by restoring the missing contact and shear waves. HLLC is quite robust and efficient but somewhat more diffusive [23]. Solution structure of HLLC approximate Riemann solver is given in Figure 3.7.

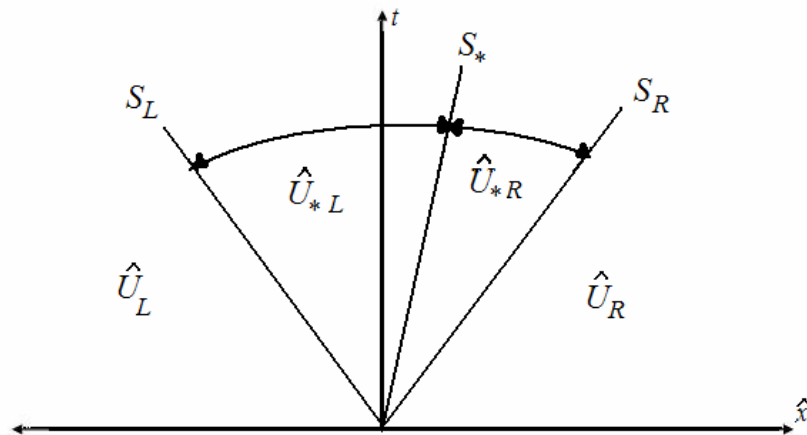


Figure 3.7 Structure of the solution of the HLLC approximate Riemann solver

For HLLC approximate Riemann solver, left hand side of Equation 3.7 is split into two parts as follows:

$$\frac{1}{TS_R - TS_L} \int_{TS_L}^{TS_R} \hat{U}(x, T) dx = \frac{1}{TS_R - TS_L} \int_{TS_L}^{TS_*} \hat{U}(x, T) dx + \frac{1}{TS_R - TS_L} \int_{TS_*}^{TS_R} \hat{U}(x, T) dx \quad (3.40)$$

The integral average, \hat{U}_{*L} , between the waves S_L and S_* is defined as

$$\hat{U}_{*L} = \frac{1}{TS_R - TS_L} \int_{TS_L}^{TS_*} \hat{U}(x, T) dx \quad (3.41)$$

The other integral average, \hat{U}_{*R} , between the waves S_* and S_R is defined as

$$\hat{U}_{*R} = \frac{1}{TS_R - TS_L} \int_{TS_*}^{TS_R} \hat{U}(x, T) dx \quad (3.42)$$

$$\begin{aligned} p_{*R} &= p_{*L} = p_* \\ \hat{u}_{*R} &= \hat{u}_{*L} = \hat{u}_* = S_* \\ \hat{v}_{*R} &= \hat{v}_R \\ \hat{v}_{*L} &= \hat{v}_L \end{aligned} \quad (3.43)$$

Integrating over the control volumes as explained in previous chapter and using the conditions given in above equation, \hat{U}_{*L} and \hat{U}_{*R} can be obtained as follows:

$$U_{*L} = \rho_L \frac{S_L - \hat{u}_L}{S_L - S_*} \begin{bmatrix} 1 \\ S_* \\ v_L \\ \frac{E_L}{\rho_L} + (S_* - \hat{u}_L) \left(S_* + \frac{\rho_L}{\rho_L (S_L - \hat{u}_L)} \right) \end{bmatrix} \quad (3.44)$$

$$U_{*R} = \rho_R \frac{S_R - \hat{u}_L}{S_R - S_*} \begin{bmatrix} 1 \\ S_* \\ v_R \\ \frac{E_R}{\rho_R} + (S_* - \hat{u}_R) \left(S_* + \frac{\rho_R}{\rho_R (S_R - \hat{u}_R)} \right) \end{bmatrix} \quad (3.45)$$

Solution procedures of \hat{U}_{*L} and \hat{U}_{*R} are given in reference [10] in details.

HLLC approximate Riemann solver assumes three wave structures so there are four separate regions. If the interface of two corresponding cells is in the left region of S_L inter-cell flux is F_L . The inter-cell flux is F_R if the interface is in the right side of the S_R . If the interface is in the region between the S_L and S_* , inter-cell flux is F_{*L} . In the region between the S_R and S_* , inter-cell flux is F_{*R} .

The inter-cell flux at a face f for the HLLC Riemann solver is given as follows: [10]

$$F_f^{HLLC} = \begin{cases} F_L & , 0 \leq S_L \\ F_{*L} = F_L + S_L (\hat{U}_{*L} - \hat{U}_L) & , S_L \leq 0 \leq S_* \\ F_{*R} = F_R + S_R (\hat{U}_{*R} - \hat{U}_R) & , S_* \leq 0 \leq S_R \\ F_R & , 0 \leq S_R \end{cases} \quad (3.46)$$

The middle wave speed S_* can be calculated using Equation 3.47 [24].

$$S_* = \frac{P_R - P_L + \rho_L \hat{u}_L (S_l - \hat{u}_L) - \rho_R \hat{u}_R (S_{lr} - \hat{u}_r)}{\rho_L (S_l - \hat{u}_L) - \rho_R (S_{lr} - \hat{u}_r)} \quad (3.47)$$

The right and left wave speeds, S_L and S_R , are calculated by using the methods presented by Davis [13] and Einfeldt [14] as mentioned in the previous section.

3.2. Evaluation of Viscous Flux

The velocity and temperature gradients over the faces are required for the evaluation of viscous fluxes. Calculation of viscous fluxes over the cells is given below

$$\frac{\Delta t}{\Delta V} \sum_{f=1}^{nf} \left(\frac{\partial F_v}{\partial x} + \frac{\partial G_v}{\partial y} \right)_f = \frac{\Delta t}{\Delta V} \sum_{f=1}^{nf} (F_v i + G_v j) \vec{n}_f \quad (3.48)$$

The velocity and temperature gradients are calculated at the cell center; however, since gradients at the cell faces are needed, the average of the gradients of the right and the left cells of a face is used as the gradients on that face. For all boundary conditions, except the wall boundary condition, velocity and temperature gradients at the cell faces are taken as the same as the gradients at the cell center.

The temperature gradient in the normal direction of the cell face is taken as zero, since adiabatic wall assumption is made.

3.3. Coordinate Transformation

Convective fluxes over the faces are calculated by using the right and left state of faces. During the calculation of fluxes, rotational invariance property of the Euler equations is used [10]. The domains that are not aligned with Cartesian coordinates can be dealt with the aid of this property. Using the rotation matrix of a face, right and left state vectors of this face are rotated to facial coordinates. Rotation matrix, T_f , of a face can be expressed as follows:

$$T_f = \begin{bmatrix} 1 & 0 & 0 & 0 \\ 0 & \cos\theta & \sin\theta & 0 \\ 0 & -\sin\theta & \cos\theta & 0 \\ 0 & 0 & 0 & 1 \end{bmatrix} \quad (3.49)$$

where θ is the angle between the normal of the face and the horizontal direction.

T_f^{-1} is the inverse rotational matrix used to rotate the vectors from facial coordinates to Cartesian coordinates. T_f^{-1} is as follows:

$$T_f^{-1} = \begin{bmatrix} 1 & 0 & 0 & 0 \\ 0 & \cos\theta & -\sin\theta & 0 \\ 0 & \sin\theta & \cos\theta & 0 \\ 0 & 0 & 0 & 1 \end{bmatrix} \quad (3.50)$$

3.4. Calculation of Time Steps

Δt is calculated for each cell using the following formula

$$\Delta t = \frac{C_{cfl} \cdot V}{A_x(|u| + a) + A_y(|v| + a)} \quad (3.51)$$

where C_{cfl} and V are the CFL number and the area of cell, respectively, a is the speed of sound in the corresponding cell, A_x and A_y are the projections of the control volume on the y axis and the x axis, respectively.

$$A_x = \frac{1}{2} \sum_{f=1}^{nf} |\vec{A}_x|_f, \quad A_y = \frac{1}{2} \sum_{f=1}^{nf} |\vec{A}_y|_f \quad (3.52)$$

where \vec{A}_x and \vec{A}_y are the x and y components of face normal, respectively.

3.5. Explicit Time Stepping

In this study, one of the most popular explicit methods, Runge-Kutta multi-stage time stepping scheme, is used for the time discretization. Four stage Runge-Kutta scheme can be given as follows.

$$\begin{aligned}U^0 &= U^n \\U^1 &= U^n + \alpha_1 \frac{\Delta t}{V} \sum_1^{nf} S_f T_f^{-1} F_f^0 \\U^2 &= U^n + \alpha_2 \frac{\Delta t}{V} \sum_1^{nf} S_f T_f^{-1} F_f^1 \\U^3 &= U^n + \alpha_3 \frac{\Delta t}{V} \sum_1^{nf} S_f T_f^{-1} F_f^2 \\U^{n+1} &= U^n + \alpha_4 \frac{\Delta t}{V} \sum_1^{nf} S_f T_f^{-1} F_f^3\end{aligned}\tag{3.53}$$

where the $\alpha_1, \alpha_2, \alpha_3$ and α_4 are the coefficients for each stage. For the first order upwind spatial discretization, the following values are recommended [4].

$$\alpha_1 = 0.0833 \quad \alpha_2 = 0.2069 \quad \alpha_3 = 0.4265 \quad \alpha_4 = 1\tag{3.54}$$

For the second order spatial discretization, recommended values are [4].

$$\alpha_1 = 0.1084 \quad \alpha_2 = 0.2602 \quad \alpha_3 = 0.5052 \quad \alpha_4 = 1\tag{3.55}$$

3.6. Data Reconstruction for High Order Accuracy

By using reconstruction, cell-centered data can be extrapolated to face centers for flux computation so that the higher order accuracy in space is obtained. Reconstruction can be achieved by using the expression given below.

$$U_f = U_c + \Delta U_c \cdot \vec{r} \quad (3.56)$$

where U_c and ΔU_c are the cell-centered value and its gradient at the cell center respectively. \vec{r} is the vector from the cell center to face centroid.

Cell-centered gradient of a cell-centered value, ΔU_c , is calculated by Green-Gauss theorem.

$$\Delta U_c = \frac{1}{V} \sum \bar{U}_f \bar{A}_f \quad (3.57)$$

In above equation, \bar{U}_f is the value of face centroid. \bar{A}_f is the face normal vector. \bar{U}_f can be given as

$$\bar{U}_f = \frac{U_{cr} + U_{cl}}{2} \quad (3.58)$$

3.6.1. Limiters

Second order upwind spatial discretization requires a limiter function in order to prevent the generation of oscillations and spurious solutions in regions of high gradients, such as shocks. Maxima in the flow field must be non-increasing, minima must be non-decreasing, and no new local extrema should be created during the advancement of the solution in time.

By using a limiter, the gradients used to reconstruct the left and right state at the faces of the control volume are reduced.

In this study, Venkatakrishnan's [25] limiter is used, which reduces the reconstructed gradient ΔU_c at the center of cell by the factor

$$\Psi_c = \min_f \begin{cases} \frac{1}{\Delta_2} \left[\frac{(\Delta_{1,\max}^2 + \varepsilon^2)\Delta_2 + 2\Delta_2^2\Delta_{c,\max}}{\Delta_{c,\max}^2 + 2\Delta_2^2 + \Delta_{c,\max}\Delta_2 + \varepsilon^2} \right] & \Delta_2 > 0 \\ \frac{1}{\Delta_2} \left[\frac{(\Delta_{c,\min}^2 + \varepsilon^2)\Delta_2 + 2\Delta_2^2\Delta_{c,\min}}{\Delta_{c,\min}^2 + 2\Delta_2^2 + \Delta_{c,\min}\Delta_2 + \varepsilon^2} \right] & \Delta_2 < 0 \\ 1 & \Delta_2 = 0 \end{cases} \quad (3.59)$$

where

$$\Delta_{c,\max} = U_{\max} - U_c \quad (3.60)$$

$$\Delta_{c,\min} = U_{\min} - U_c \quad (3.61)$$

In the above equations, U_{\max} and U_{\min} stand for the maximum and minimum values of all surrounding cells including the corresponding cell. Definition of Δ_2 is given by the following equation as

$$\Delta_2 = \Delta U \bar{r} \quad (3.62)$$

where \bar{r} is given as the vector from the cell centroid to the midpoint of the corresponding cell face.

The parameter ε^2 is intended to control the amount of limiting. In practice, ε^2 is taken to be proportional to a local length scale;

$$\varepsilon^2 = (\kappa_v \Delta h)^3 \quad (3.63)$$

where κ_v is a constant and Δh is the square-root of the area of the cell for two dimensional case.

3.7. Boundary Conditions

3.7.1. Inviscid Wall Boundary Condition

In an inviscid wall boundary, a ghost cell is used. State of a ghost cell is calculated as follows.

$$U_G = \begin{bmatrix} \hat{\rho}_d \\ -\hat{\rho}_d \hat{u}_d \\ \hat{\rho}_d \hat{v}_d \\ \hat{E}_d \end{bmatrix} \quad (3.64)$$

All values in above equation are the values which are rotated from Cartesian coordinates to facial coordinates.

3.7.2. Viscous Wall Boundary Condition

For the viscous wall boundary, state of a ghost cell is assumed as follows.

$$U_G = \begin{bmatrix} \hat{\rho}_d \\ -\hat{\rho}_d \hat{u}_d \\ -\hat{\rho}_d \hat{v}_d \\ \hat{E}_d \end{bmatrix} \quad (3.65)$$

The velocity components of a ghost cell in facial coordinates are the negative of those of domain cells. Gradients of this boundary can be calculated as follows:

$$\frac{\partial \hat{u}}{\partial \hat{x}} = \frac{\hat{u}}{\Delta \hat{x}} \quad (3.66)$$

$$\frac{\partial \hat{v}}{\partial \hat{x}} = \frac{\hat{v}}{\Delta \hat{x}} \quad (3.67)$$

$$\frac{\partial \hat{u}}{\partial \hat{y}} = 0 \quad (3.68)$$

$$\frac{\partial \hat{v}}{\partial \hat{y}} = 0 \quad (3.69)$$

where $\Delta \hat{x}$ is the distance between the cell center and face center.

3.7.3. Far Field Boundary Condition

The state of a face on the far field boundary depends on the direction and speed of the flow in facial coordinates. In a boundary, there are two basic situations, inflow and outflow. One of the following four far field boundary types occurs depending on the local Mach number.

1. Supersonic Inflow

2. Subsonic Inflow
3. Supersonic Outflow
4. Subsonic Outflow

1. Supersonic inflow

For the supersonic inflow case, states of boundary faces are determined from the free stream values.

2. Subsonic inflow

If the flow is subsonic and entering into the domain, one of the characteristic variables is extrapolated from the domain while the other ones are taken from the freestream values.

$$p_f = \frac{1}{2}(p_\infty + p_d - \rho_d a_d (\hat{u}_\infty - \hat{u}_d))$$

$$\rho_f = \rho_\infty + \frac{(p_f - p_\infty)}{a_d^2} \quad (3.70)$$

$$\hat{u}_f = \hat{u}_\infty + \frac{(p_f - p_\infty)}{\rho_d a_d} \quad \hat{v}_f = 0$$

3. Supersonic outflow

In the case of supersonic outflow, states of boundary faces are determined by the extrapolation from the corresponding values into the domain.

4. Subsonic outflow

If the far field boundary type is subsonic outflow, pressure is taken from the free stream and the other ones are determined by the extrapolation from the corresponding values into the domain.

$$p_f = p_\infty$$

$$\rho_f = \rho_d + \frac{(p_f - p_d)}{a_d^2} \quad (3.71)$$

$$\hat{u}_f = \hat{u}_d + \frac{(p_d - p_f)}{\rho_d a_d} \quad \hat{v}_f = 0$$

3.7.4. Mass Flow Inlet Boundary Condition

Mass flow boundary condition can be used to provide a prescribed mass flow rate at a boundary. Mass flux, total temperature and the static pressure are provided. The mass flux is always in a direction into the domain and its value is $\hat{\rho}\hat{u}$. Density is calculated with the procedure described below.

For an ideal gas, density ρ is calculated using static pressure p and static temperature T by the following expression.

$$\rho = \frac{p}{RT} \quad (3.72)$$

In the mass flow inlet boundary conditions, the total temperature T_0 is to be provided. Total and static temperatures are related by

$$\frac{T_0}{T} = 1 + \frac{(\gamma - 1)\hat{u}^2}{2a^2} \quad (3.73)$$

The sound speed, a and the normal velocity, \hat{u} , can be expressed as

$$a = \sqrt{\frac{\gamma p}{\rho}} \quad \hat{u} = \frac{\dot{m}}{\rho} \quad (3.74)$$

Using equations 3.72, 3.73 and 3.74, one can obtain the following formula for the density.

$$\rho = \frac{\gamma p + \sqrt{\gamma} \sqrt{2R\dot{m}^2(\gamma-1)T_0 + \gamma p^2}}{2a^2} \quad (3.75)$$

3.7.5. Pressure Outlet Boundary Condition

In pressure outlet boundary conditions, static pressure at the boundary is specified. All flow variables at the faces of pressure outlet boundary are taken from the domain in supersonic flow regime at the boundary. In the case of subsonic regime, all flow variables except the pressure are taken from domain, while the pressure at the face, p_f , is calculated as [26]

$$p_f = p^+(M_n)p_D + p^-(M_n)p_B \quad (3.76)$$

where p_D and p_B are the domain pressure and the boundary pressure, respectively. p^+ and p^- can be given as follows:

$$p^\pm(M_n) = \begin{cases} \frac{1}{M_n} M_1^\pm & \text{if } |M_n| \geq 1 \\ M_2^\pm (\mp 2 - M_n) \mp 16\alpha M_n M_2^\mp & \text{if } |M_n| \leq 1 \end{cases} \quad (3.77)$$

where α is 3/16 [6]. M_1^\pm and M_2^\pm are calculated as follows:

$$M_1^\pm = \frac{1}{2}(M_n \pm |M_n|) \quad (3.78)$$

$$M_2^\pm = \pm \frac{1}{4}(M_n \pm 1)^2 \quad (3.79)$$

3.7.6. Axisymmetric Boundary Condition

Implementation of the axisymmetric boundary condition is the same as the inviscid boundary conditions. If there is an axisymmetric boundary condition in the domain, axisymmetric source term should be added to the calculated residuals of each cell. Axisymmetric Navier-Stokes equations are as follows:

$$\frac{\partial U}{\partial t} + \frac{\partial(F - F_v)}{\partial x} + \frac{\partial(G - G_v)}{\partial y} = S(U) \quad (3.80)$$

where

$$S = -\frac{1}{r} \begin{bmatrix} \rho v \\ \rho v u \\ \rho v v + p \\ \nu(E + p) \end{bmatrix} \quad (3.81)$$

In axisymmetric flows, cells and faces can be assumed to be rotated around the symmetry axis to produce three dimensional cells and faces. If these three dimensional cells and faces are used to solve the problem, it is not necessary to calculate source term, S . Cell volumes and face areas are calculated by using following equations, respectively, since they are three-dimensional.

$$V_c = 2\pi r_c A_c \quad (3.82)$$

$$A_f = 2\pi r_c L_f \quad (3.83)$$

In the above equations, r_c is the distance from the cell center to the symmetry axis. Using V_c and A_f , the solution procedure is the same as the two-dimensional case. But in this case, a new source term should be considered which is given as follows; [27], [28].

$$S = -\frac{1}{r} \begin{bmatrix} 0 \\ 0 \\ P \\ 0 \end{bmatrix} \quad (3.84)$$

CHAPTER 4

TEST CASES AND RESULTS

Test cases and the results of the solver are presented in this chapter. There are 5 case solved for the validation of the present numerical methods solving the Euler equations and the Navier-Stokes equations.

The accuracy of approximate Riemann solvers, HLL and HLLC, are tested by cylindrical explosion. Results are compared with the exact solution and the results of WAF-HLL method obtained from the reference [10]. First order and second order special accuracy is validated by solving the flow over a circular bump. Result from reference [29] is used for the validation of this test case. Axisymmetric flow solving capability is tested by the third test case which is the inviscid flow in SPRM. Reference [31] is used to validate this case. The overall solution algorithm and discretization accuracy of viscous flux vector is tested by solving laminar flow over a flat plate. Numerical results are then compared with the analytical solution. After validation of the viscous terms for laminar flows, implementation of the turbulence model is tested. Transition location is fixed in the turbulence test case. Solution in the laminar portion as well as in the turbulent region is compared with the analytical results.

4.1. Cylindrical Explosion

This test problem is used to validate the solver part of program. The solution domain is a 2x2 square. A circular high pressure region having a radius of $R=0.4$ is located at the center of the square. The region outside the circular region has a low pressure. This case may be called 2-D shock problem. Initially the flow variables take constant values in each zone and joined by a circular discontinuity at the zone boundaries at time $t= 0$ as shown in Figure 4.1. The initial two constant states for this problem are chosen to be

$$\begin{aligned} p_{in} &= 1 \text{ Pa} & p_{out} &= 0.1 \text{ Pa} \\ \rho_{in} &= 1 \text{ kg/m}^3 & \rho_{out} &= 0.125 \text{ kg/m}^3 \\ u_{in} &= 0 & v_{in} &= 0 & u_{out} &= 0 & v_{out} &= 0 \end{aligned} \quad (4-1)$$

Subscripts *in* and *out* denote the values inside and outside of the circle respectively. . This case was also solved by using a hybrid mesh consisting of triangle and quadrilateral grids as shown in Figure 4.2.

The variation of the pressure, velocity component in x -direction and density are given in Figure 4.3, Figure 4.4 and Figure 4.5, respectively, for the cross-section between the points $(x=1, y=1)$ and $(x=2, y=1)$. . The variation of the pressure, velocity component in x -direction and density for the hybrid grid are presented in Figure 4.6, Figure 4.7 and Figure 4.8, respectively.

When the explosion starts or diaphragm between the high pressure and low pressure region suddenly burst, a shock wave propagates through the outer region. The velocity, pressure and density increase in the outer region. After starting of explosion, a rarefaction wave is propagated through the inner region. Across this rarefaction wave, the velocity, pressure and density of the outer region gas decrease. The solution exhibits a circular shock wave traveling away from the center, a circular contact surface traveling in the same direction and a circular rarefaction traveling toward the origin as expected.

As observed from the figures, there is shock wave at $x \sim 1.8$, contact surface at $x \sim 1.6$ and a rarefaction wave at $x \sim 1.1$. In hybrid mesh, there is fine mesh in the contact region between inner and outer regions. So the waves are more evident than the previous one. In those figures, the results labeled Random Choice Method (RCM) and Weight Averaged Flux-HLL (WAF_HLL) are taken from the reference [1]. RCM method can be thought as an exact result of the problem. Details about this problem can be seen in reference [10]. Computed results are compatible to the results of RCM and WAF_HLL.

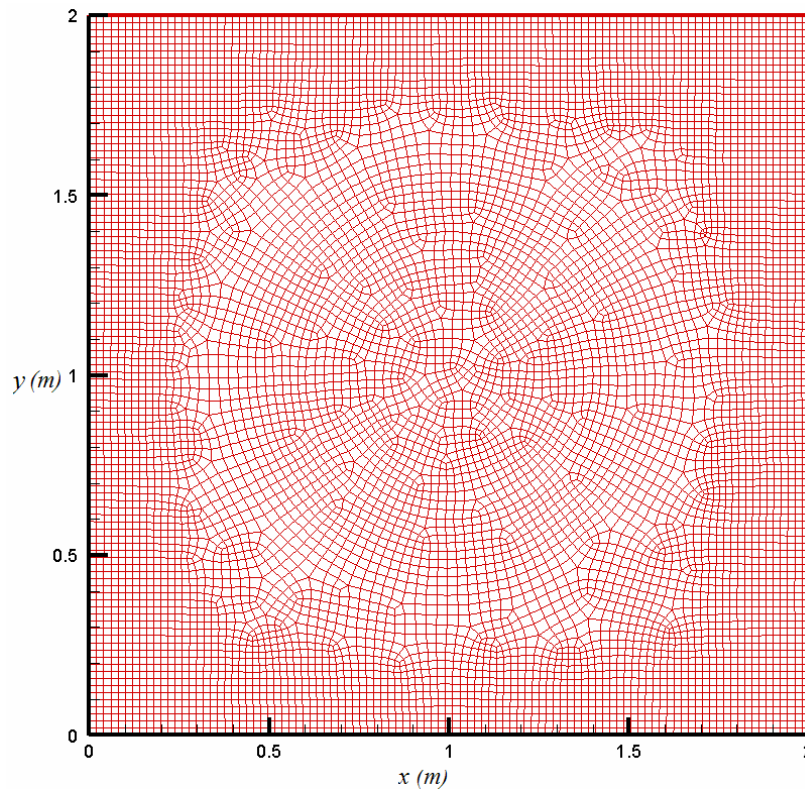


Figure 4.1 Unstructured quadrilateral mesh for the cylindrical explosion

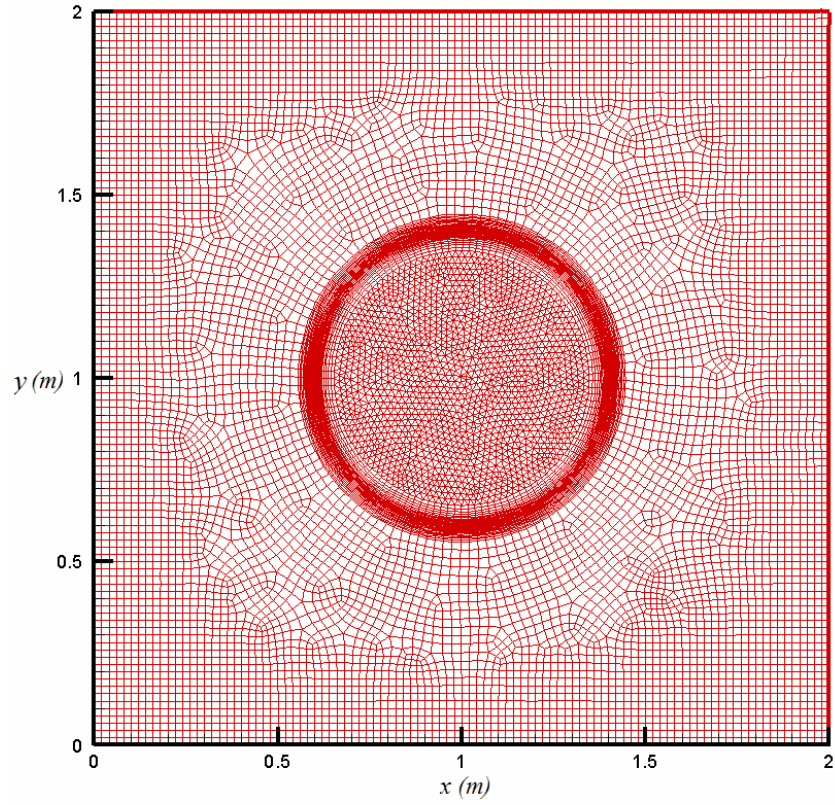


Figure 4.2 Unstructured triangular and quadrilateral mesh for the cylindrical explosion

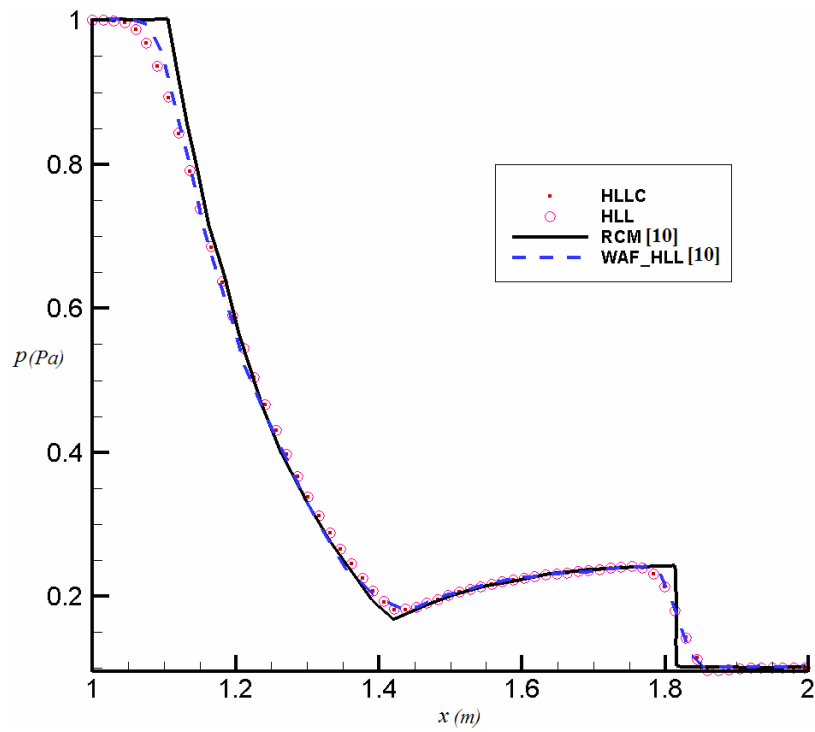


Figure 4.3 Pressure distribution at $t=0.25$ s. for the quadrilateral mesh

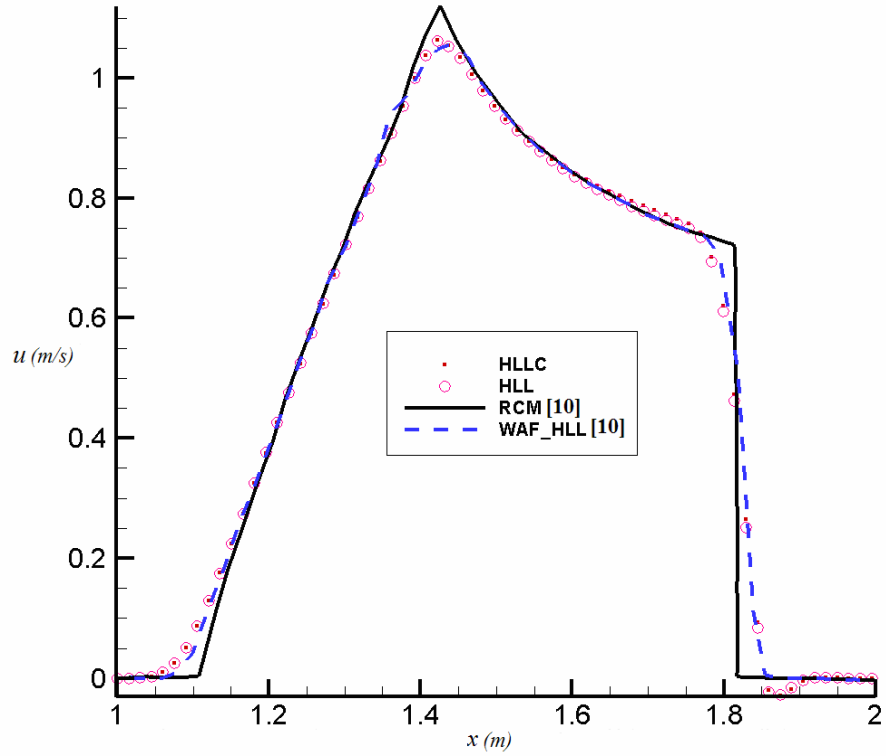


Figure 4.4 Distribution of the axial velocity at $t=0.25$ s. for the quadrilateral mesh

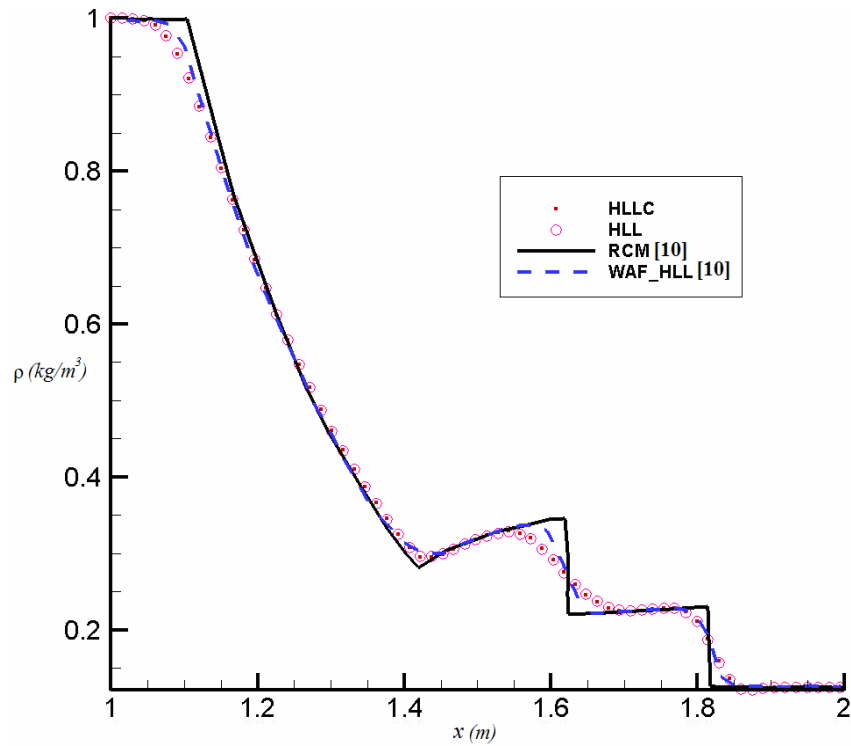


Figure 4.5 Density distribution at $t=0.25$ s.

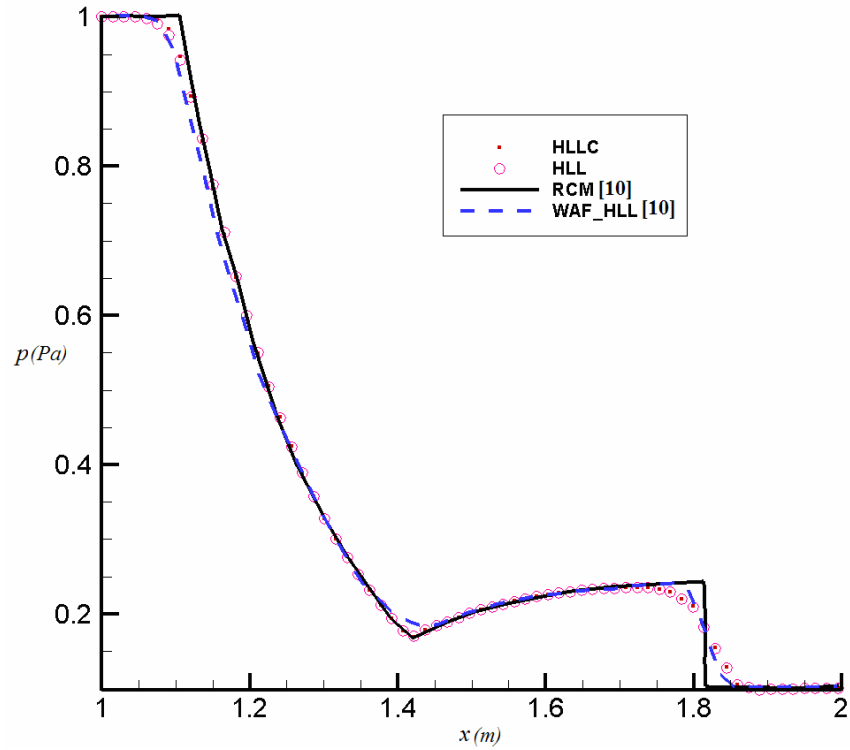


Figure 4.6 Pressure distribution at $t=0.25$ s. for the hybrid grid

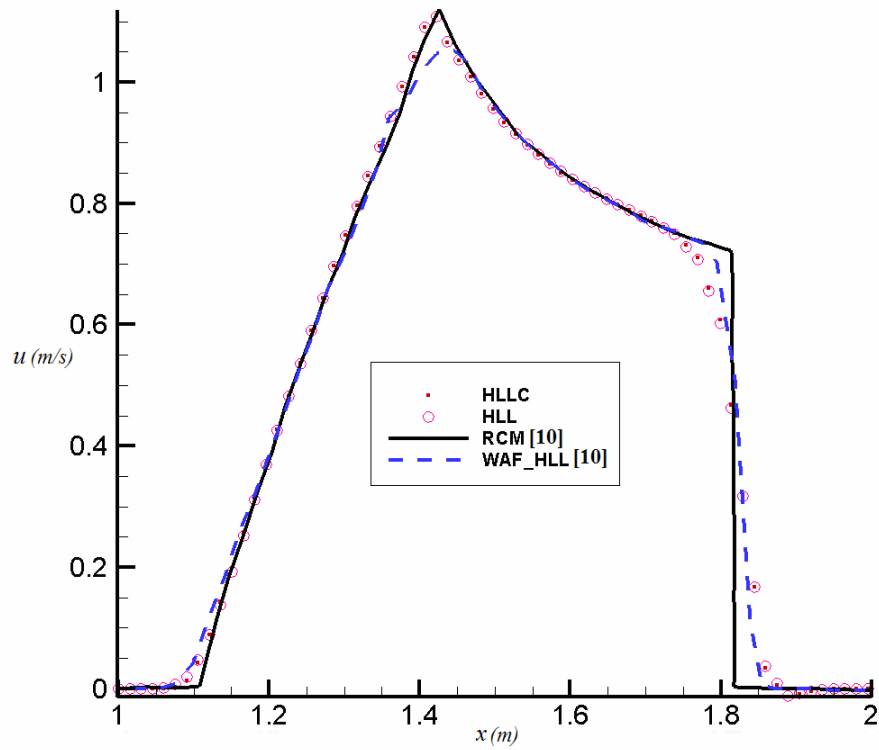


Figure 4.7 Distribution of the axial velocity at $t=0.25$ s. for the hybrid grid

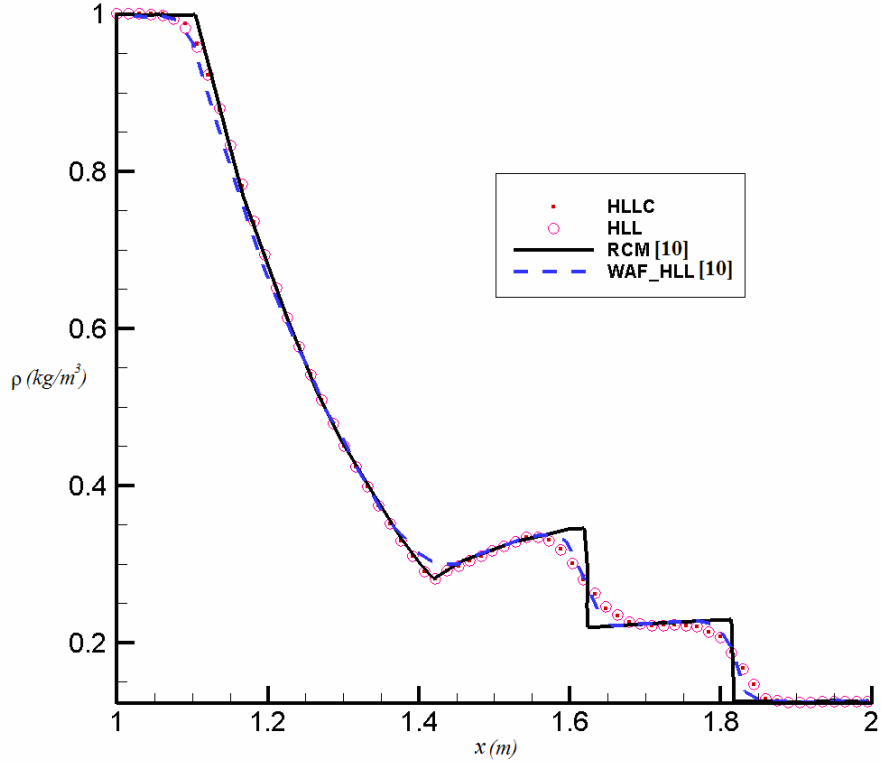


Figure 4.8 Density distribution at $t=0.25$ s. for the hybrid grid

4.2. Flow over a Circular Bump

This test case is used to validate the second order accuracy of the spatial discretisation used in the code. The geometry used for this problem consists of a bump having a thickness of 4% of the chord length. Computational domain consists of triangular grids as shown in Figure 4.9.

Inviscid wall boundary is implemented to the upper and lower boundaries. Outlet boundary is defined as pressure outlet boundary having a pressure value of 101325 Pa. Mass flow inlet boundary condition is implemented for the inlet boundary. Values for the mass flow inlet boundary condition are given as follows:

$$\begin{aligned} \dot{m} &= 571.9 \text{ kg/s/m}^2 \\ T_o &= 417.3 \text{ K} \end{aligned} \tag{4-2}$$

$$p = 101325 \text{ Pa}$$

Mach number distribution on the upper and the lower wall given in Figure 4.10 and Figure 4.13 are compared with the Mach number distribution obtained by using HLL method and weight average flux HLL method presented in reference [29] and the Mach number distribution taken from reference [30].

There are two oblique shock waves at the leading and trailing edges of the bump. A shock is generated as flow reaches the bump. This shock is reflected by the upper wall then crosses the shock which issues from the end of the bump. The two shocks meet again before exiting the supersonic channel. Mach contours obtained with HLL and HLLC methods with the first and the second order spatial accuracy are shown in Figure 4.11, Figure 4.12, Figure 4.14, and Figure 4.15, respectively. For the first order spatial accuracy, those oblique shocks can not be captured very well. But for the second order spatial accuracy oblique shocks are captured well than the one obtained by using the first order spatial accuracy.

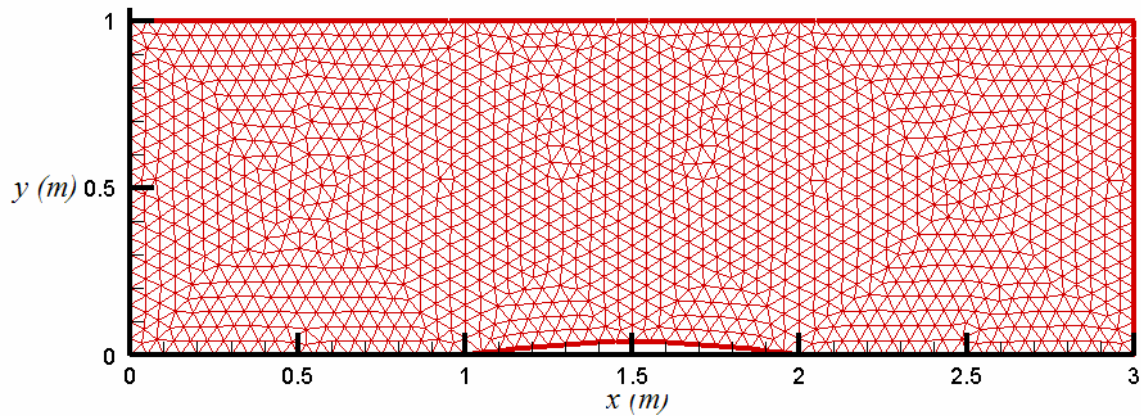


Figure 4.9 Grid for flow over circular bump problem

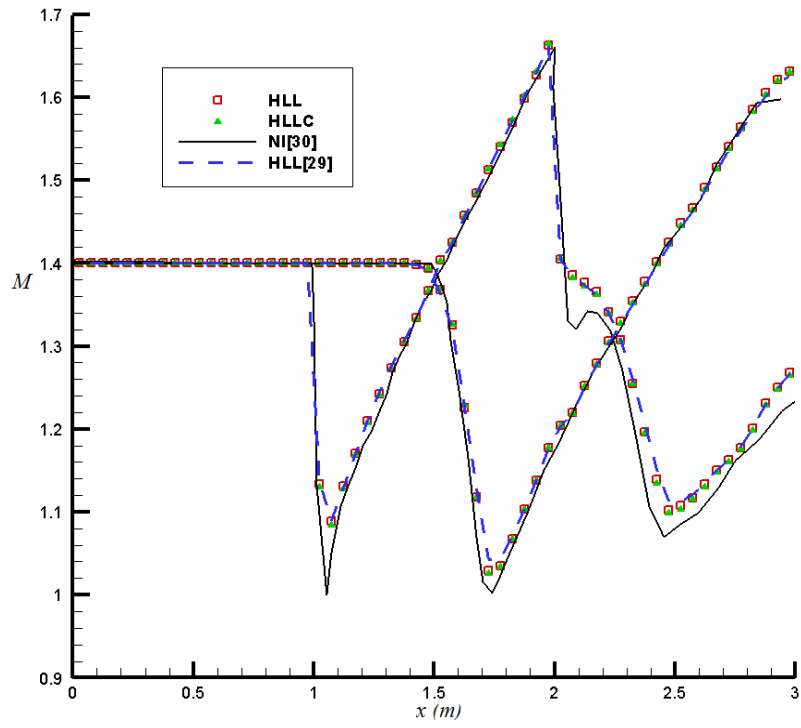


Figure 4.10 Distribution of Mach number for first order spatial accuracy

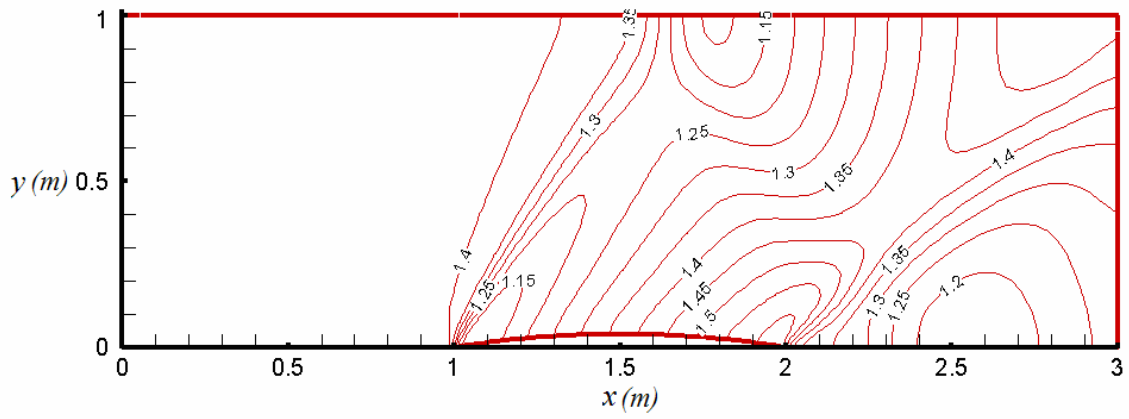


Figure 4.11 Mach number contour for first order spatial accuracy with HLL method

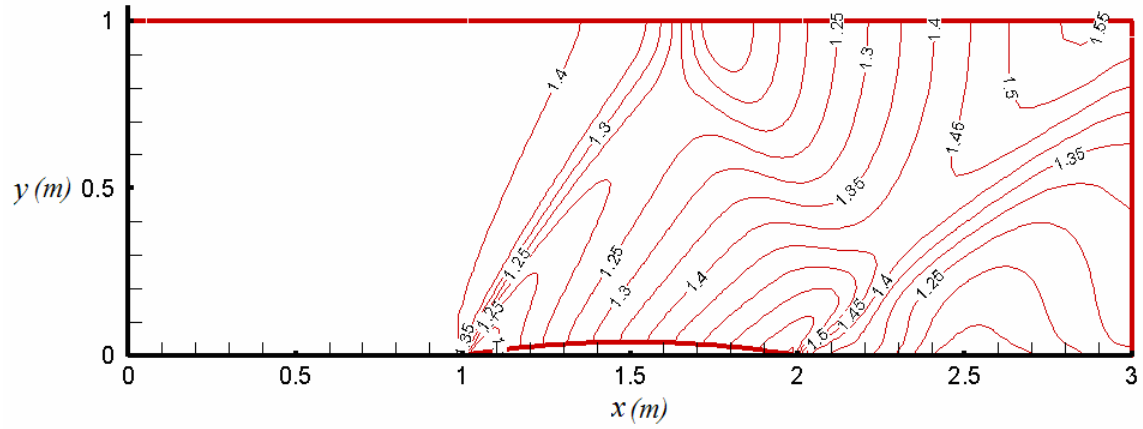


Figure 4.12 Mach number contour for first order spatial accuracy with HLLC method

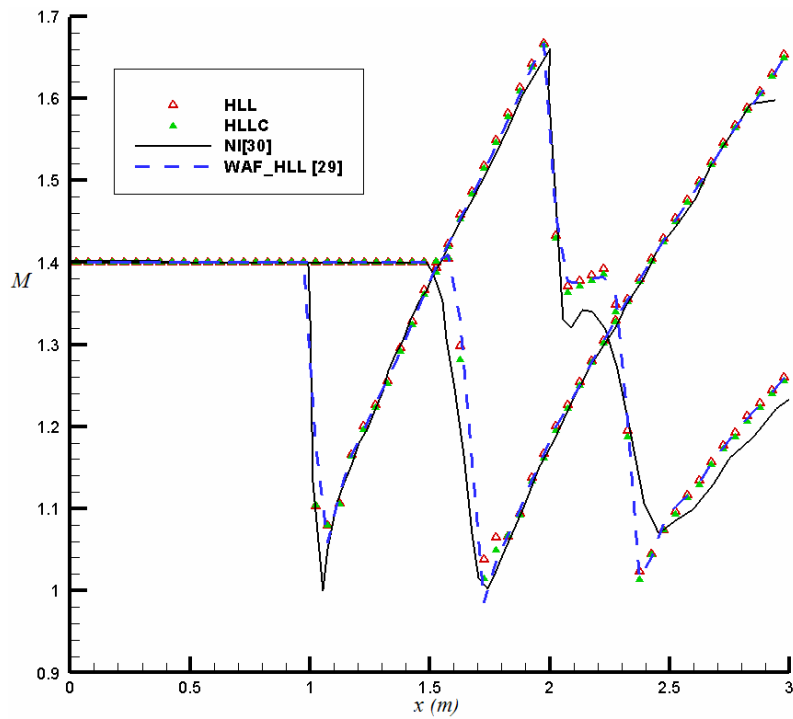


Figure 4.13 Distribution of Mach number for second order spatial accuracy

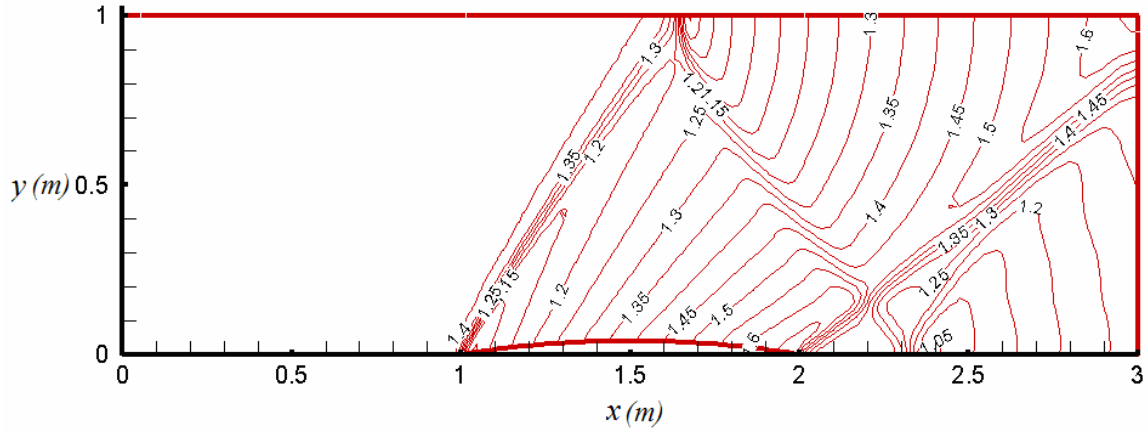


Figure 4.14 Mach number contour for second order spatial accuracy with HLL method

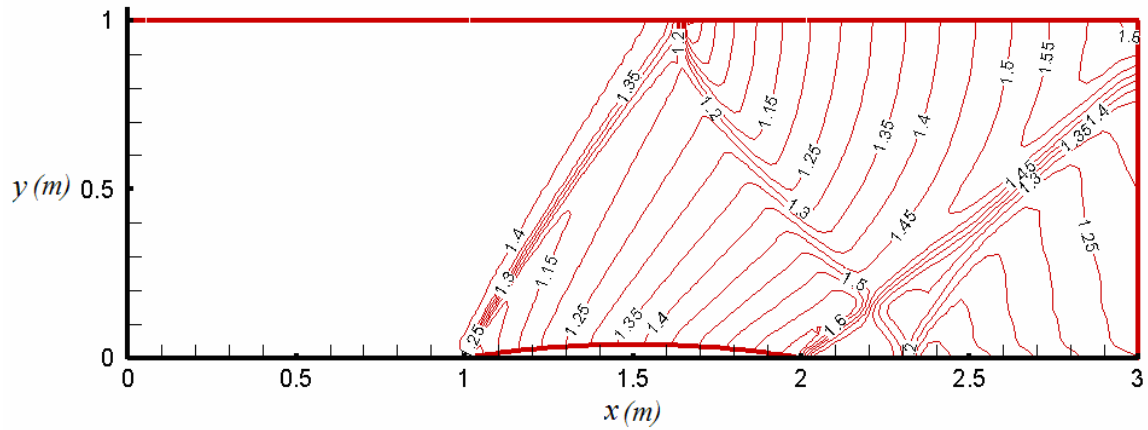


Figure 4.15 Mach number contour for second order spatial accuracy with HLLC method

4.3. Inviscid Axisymmetric Flow in SPRM

This test case is studied for the verification of mass injection boundary condition and axisymmetric problem solving capability of the developed code. Flow in a SPRM which has been used in reference [31] to validate the stability of 2-D computations is solved in this case. For this test case, a grid consisting of 196x30 cells is used as given in Figure 4.16. Upper wall has a length of 170 mm and a radius of 45 mm. SPRM has a converging-diverging nozzle which has a throat diameter of 16.7 mm. Motor length is

270 mm. The mass is injected from the upper wall at a constant temperature. Values for the mass flow inlet boundary condition are given as follows:

$$\begin{aligned} \dot{m} &= 11.39 \text{ kg/s/m}^2 \\ T_o &= 3387 \text{ K} \\ p &= 101325 \text{ Pa} \end{aligned} \quad (4-3)$$

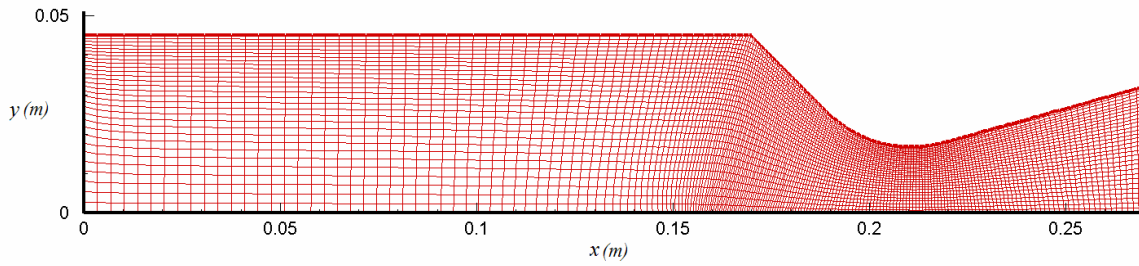


Figure 4.16 Mesh used for SPRM

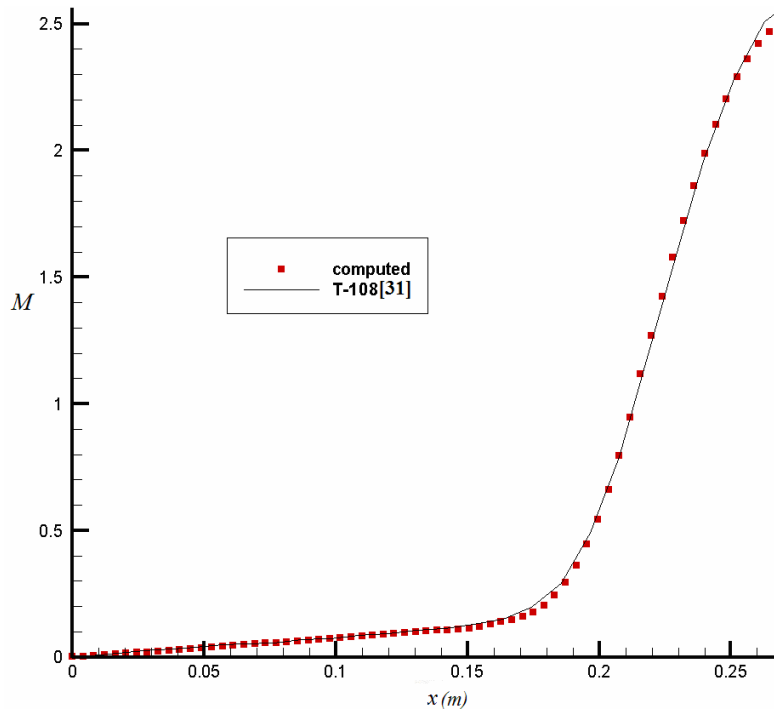


Figure 4.17 Mach number along the symmetry axis

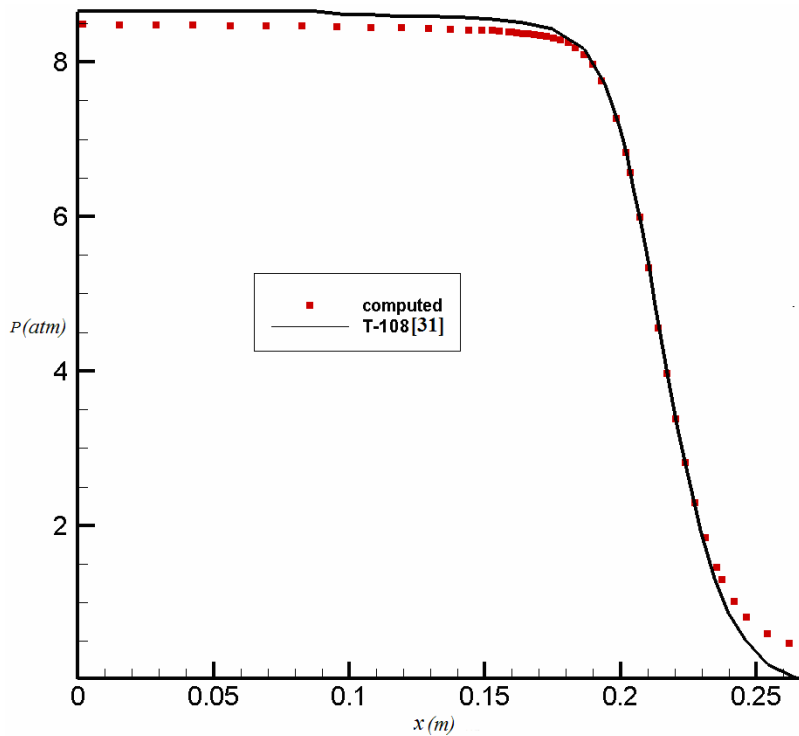


Figure 4.18 Pressure (atm) along the symmetry axis

Mach number and pressure variation along the symmetry axis are given in Figure 4.17 and Figure 4.18, respectively. Results labeled as T-108 are taken from reference [31]. Computed results are well suited with the T-108 results. Mach number is increasing in the converging part of the nozzle as expected and takes the value of 1 at the throat. At the diverging part, the flow is supersonic. At the exit plane, Mach number reaches a value of about 2.5. Pressure is almost the constant in the motor up to the converging part. It takes its maximum value of 2.77 MPa at the head end of the motor.

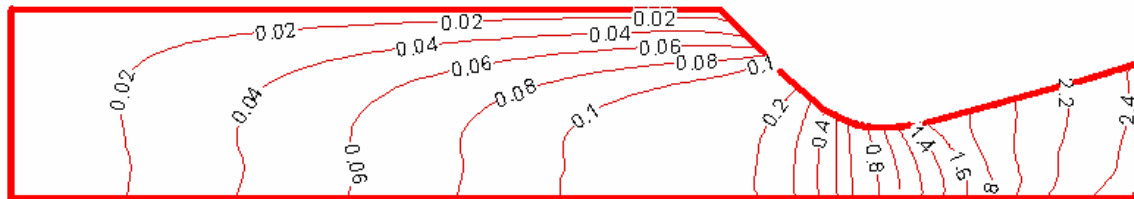


Figure 4.19 Mach contour of SPRM

4.4. Laminar Flow over a Flat Plate

In order to verify the viscous terms in the developed code, laminar flow over a flat plate is analyzed. Values of free stream are given as follows:

$$\begin{aligned}u_{\infty} &= 32.9 \text{ kg/s/m}^2 \\T_{\infty} &= 3000 \text{ K} \\p_{\infty} &= 101325 \text{ Pa}\end{aligned}\tag{4-4}$$

The free stream Reynolds number of the flow is 50500. A grid consisting of 141x61 cells is used as shown in Figure 4.20. First Δy is taken as 0.0001 and it exponentially grows up to the top of the boundary. At the leading edge of flat plate, at $x = 2$, Δx is 0.00035. Fine mesh at the leading edge is necessary to handle the gradients in this region. There are 70 nodes upstream on the symmetry surface, 56 nodes on the flat plate and 15 nodes in the downstream region. Flat plate is assumed to be placed between the points $x = 2, y = 0$ and $x = 3, y = 0$. Far-field boundary condition is used for left, upper and right sides of the grid. On the bottom side, symmetry boundary condition is used for the upstream and downstream side of the flat plate.

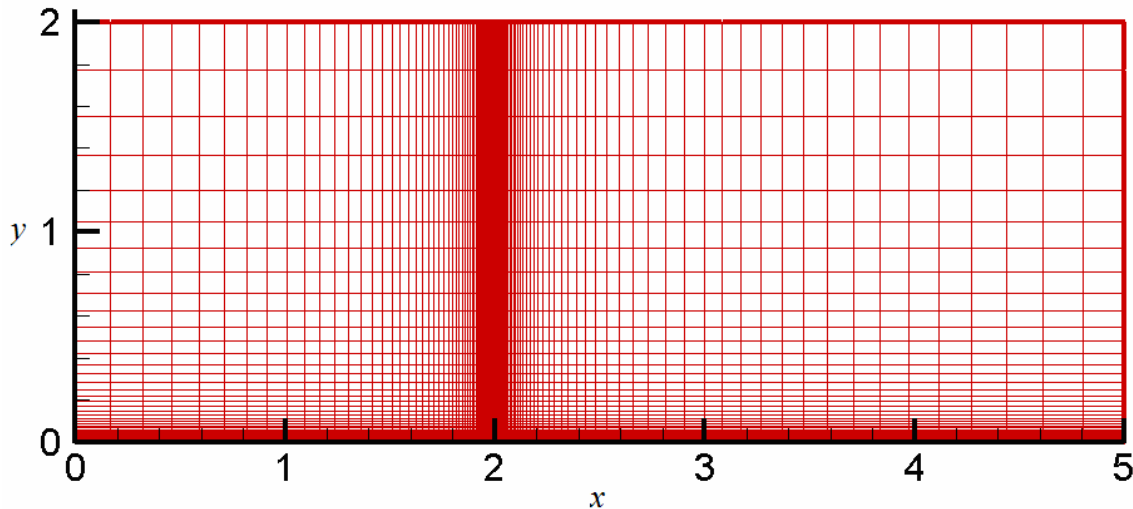


Figure 4.20 Grid used for the laminar flow over a flat plate

Velocity profiles are presented by using the similarity parameter $\eta = y \frac{\sqrt{\text{Re}_x}}{x}$.

Comparison of the tangential velocity profile with the Blasius solution is presented in Figure 4.21. Tangential velocity is found to be in good agreement with the Blasius solution. Similarly normal velocity profile compares well with the Blasius solution. In Figure 4.22, the normal velocity profile in comparison with the Blasius solution is given.

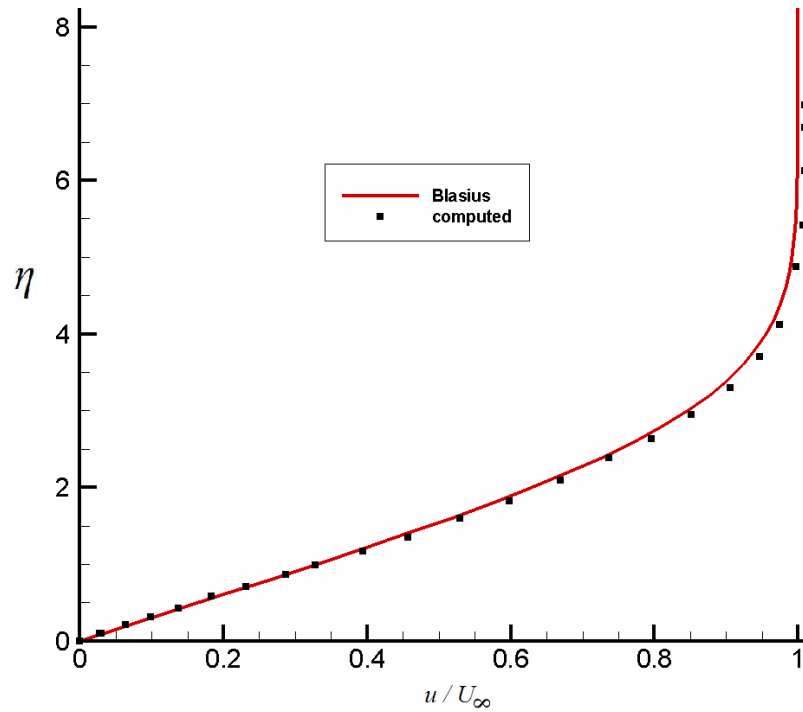


Figure 4.21 Comparison of tangential velocity profile with Blasius solution at $x/c=0.5$

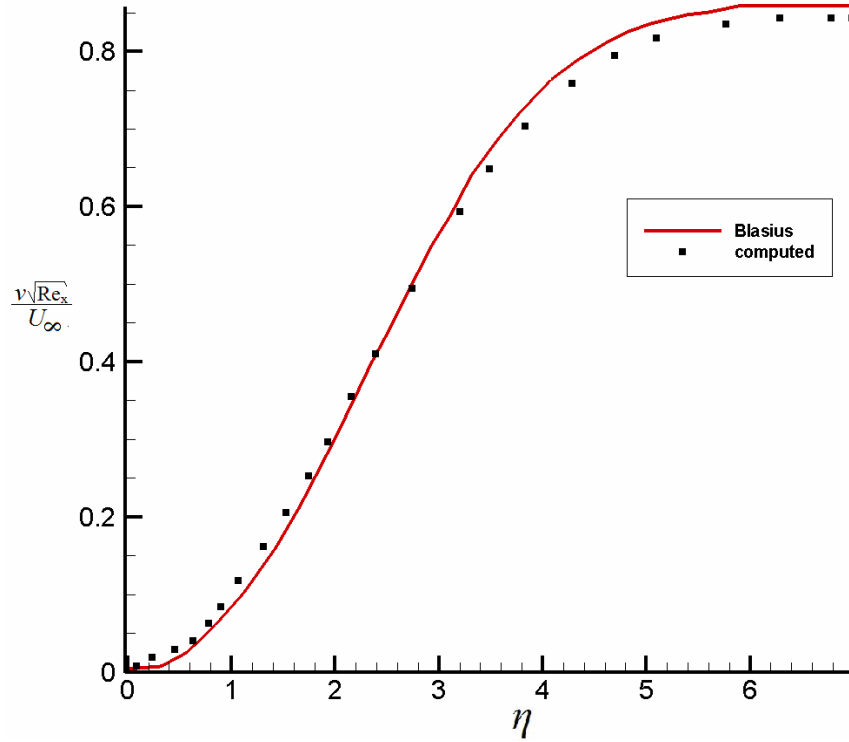


Figure 4.22 Comparison of normal velocity profile with Blasius solution at $x/c=0.5$
 Local skin friction (C_f) result along the flat plate is given in Figure 4.23. C_f is compared with the analytical solution which is given as follows:

$$C_f = \frac{0.664}{(\text{Re}_x)^{0.5}} \quad (4.5)$$

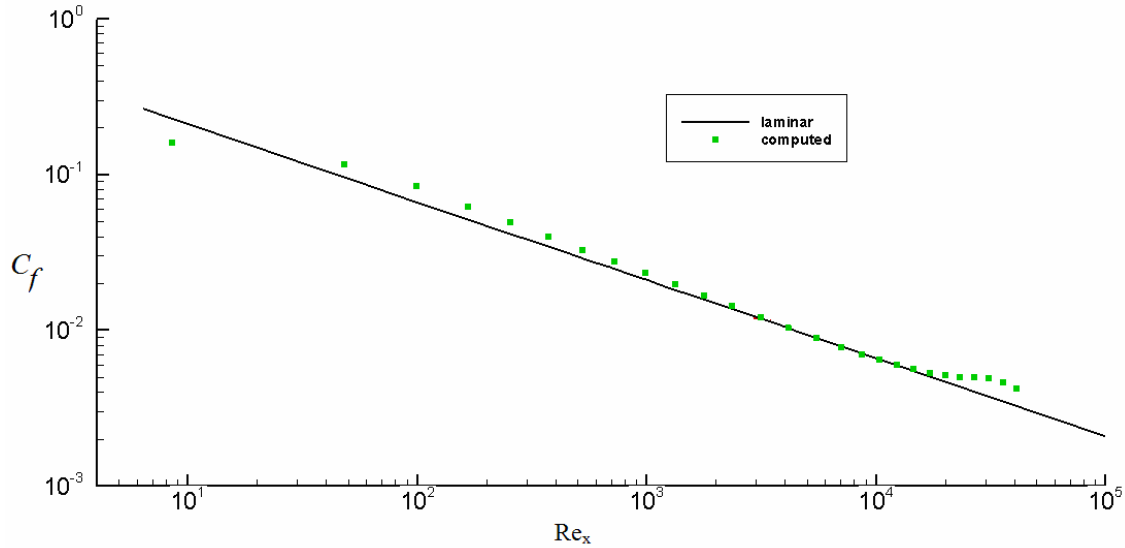


Figure 4.23 Comparison of skin friction coefficient with the analytical solution at $x/c=0.5$

The results given in Figure 4.21, Figure 4.22, and Figure 4.23 can be considered to be acceptable comparing to analytical solutions.

4.5. Turbulent Flow over a Flat Plate

Verification of turbulence model implemented in the program is carried out by a laminar-turbulence flow over a flat plate. Values of free stream are given as follows:

$$\begin{aligned}
 u_{\infty} &= 132 \text{ kg/s/m}^2 \\
 T_{\infty} &= 365 \text{ K} \\
 p_{\infty} &= 101325 \text{ Pa}
 \end{aligned}
 \tag{4-6}$$

The free stream Reynolds number of the flow is 6×10^6 . Grid consisting of triangular cells and boundary layer is used. Fine mesh on the flat plate is necessary for solving the boundary region accurately. So the first Δy is taken as 5×10^{-6} and it exponentially grows up to the top of the boundary. At the leading edge of flat plate, at $x=2$, Δx could be taken as 1×10^{-2} in order to use hybrid mesh. There are 50 nodes upstream on the symmetry

surface, 25 nodes on the flat plate and 38 nodes in the downstream region. Boundary conditions are the same as the laminar flow over a flat plate problem. Hybrid mesh used in this problem is given in Figure 4.24

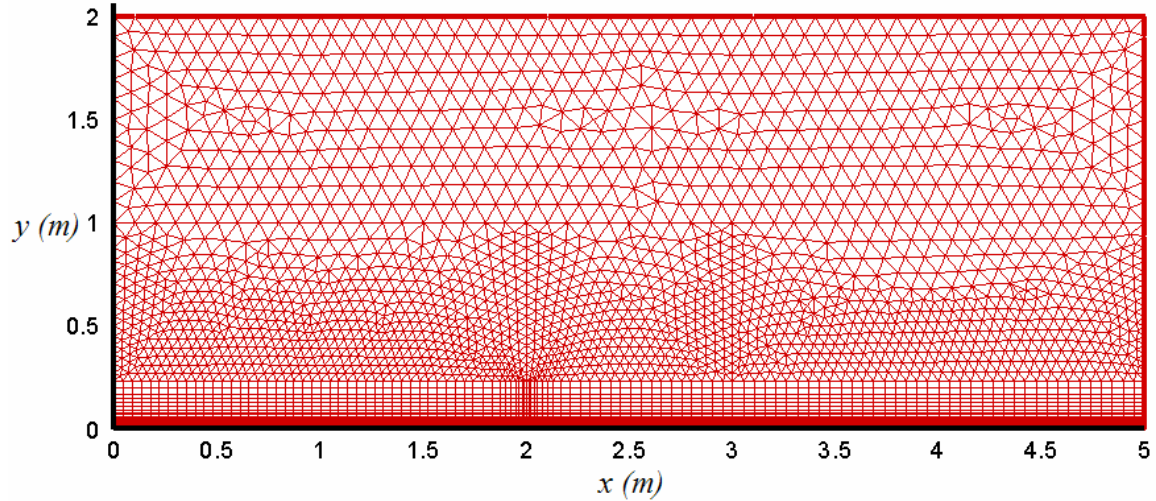


Figure 4.24 Hybrid mesh consisting of triangular cells and boundary layer

This case is also solved by using structured grid consisting of 181×81 cells. The first Δy is taken as 5×10^{-6} and it exponentially grows up to the top of the boundary. At the leading edge of flat plate, at $x=2$, Δx is 8×10^{-5} . There are 75 nodes upstream on the symmetry surface, 81 nodes on the flat plate and 25 nodes in the downstream region. Structured grid is given in Figure 4.25.

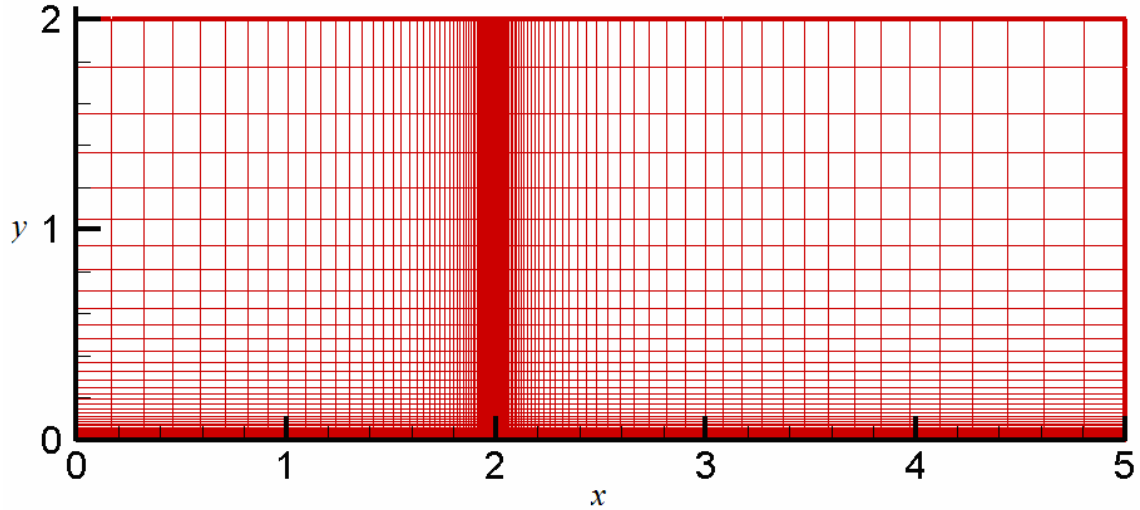


Figure 4.25 Structured grid consisting of quadrilateral cells and boundary layer

The results of this case for hybrid mesh are given in Figure 4.26, Figure 4.27, and Figure 4.28. Results obtained for skin friction coefficients by using hybrid and structured mesh are compared in Figure 4.29.

In Figure 4.26, the axial velocity of turbulent region is compared with the turbulent 1/7 law given as follows:

$$\frac{u}{U} = \left(\frac{y}{\delta}\right)^{1/7} \quad (4.7)$$

Figure 4.27 shows the similarity profiles at different locations on the flat plate. Transition point is defined as $x/c=0.054$ for this problem.

Local skin friction (C_f) result along the flat plate is given in Figure 4.28. C_f is compared with the analytical solution which is given as follows:

$$C_f = \frac{0.0592}{(\text{Re}_x)^{0.2}} \quad (4.8)$$

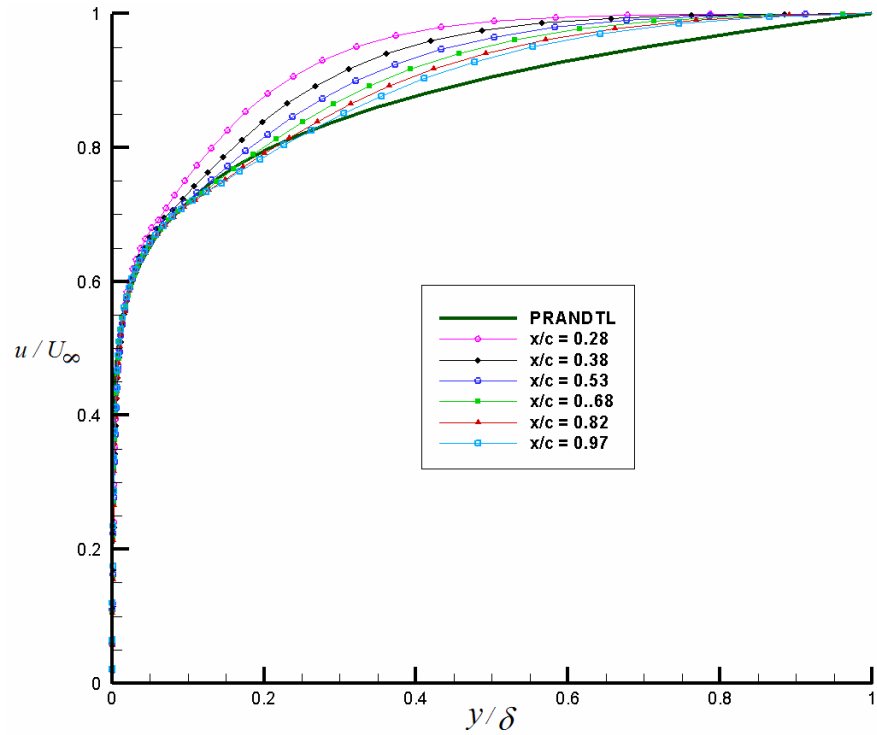


Figure 4.26 Comparison of tangential velocity profile with Prandtl's turbulent solution

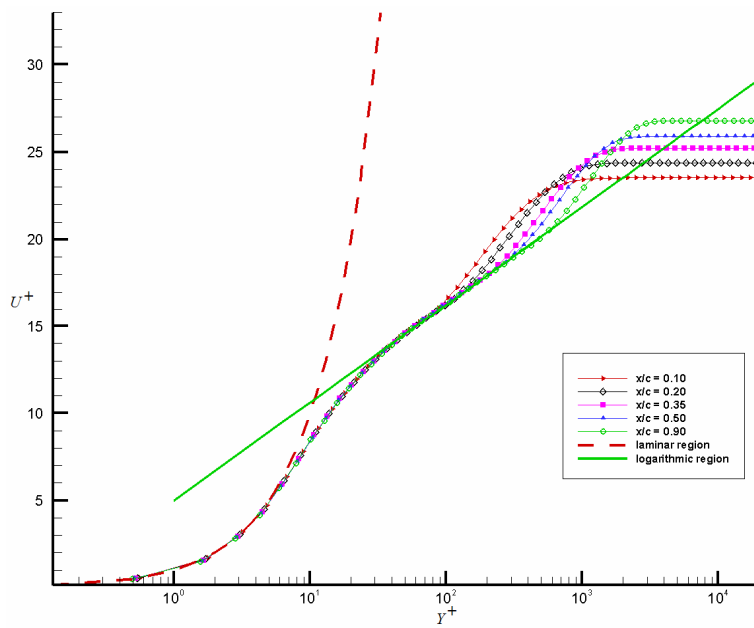


Figure 4.27 Turbulent similarity profiles for different location

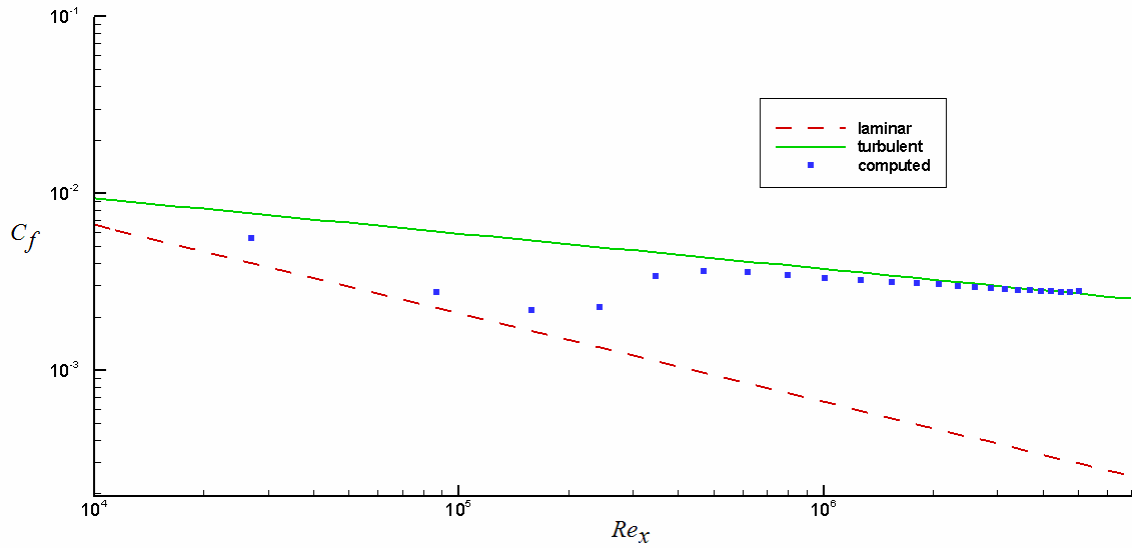


Figure 4.28 Comparison of skin friction coefficient with the analytical solution

Comparison of skin friction coefficients of hybrid and structured grid is given in Figure 4.29. In structured grid, fine mesh can be used at the leading edge of the flat plate so the region before the transition can be resolved more accurate in structured grid as can be seen in Figure 4.29.

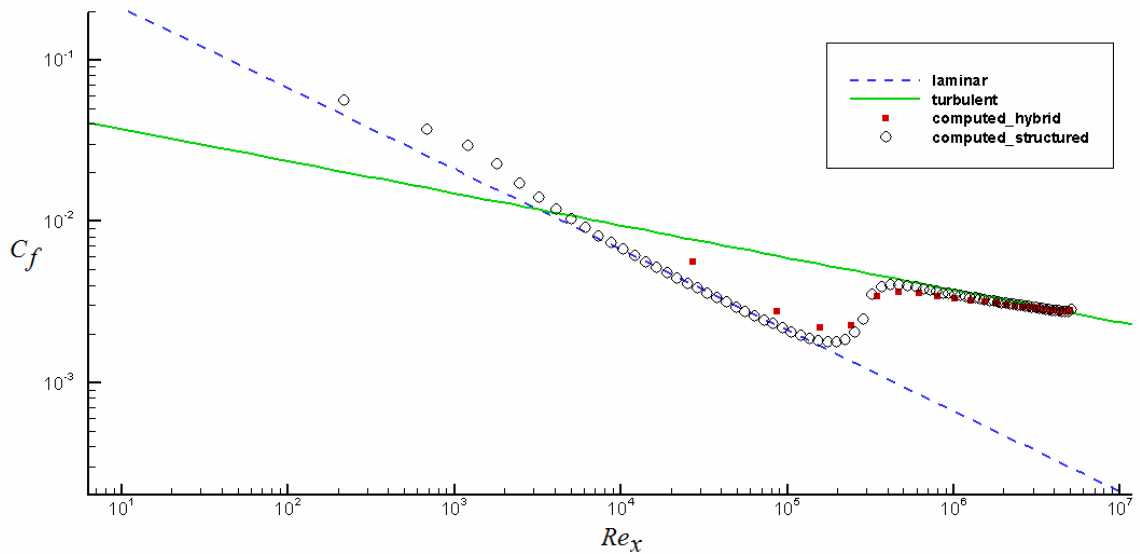


Figure 4.29 Comparison of skin friction coefficient for hybrid and structured grid

4.6. Turbulent Flow with Mass Injection

This case is solved as laminar and turbulent flows. Laminar results are compared with the turbulent results and the analytical solutions determined by the laminar incompressible similarity theory as given in Equation 4.9. Turbulent results are compared with the data obtained from a two dimensional planar experimental setup, called VECLA [32], [33], that is composed of parallel piped channel bounded by a porous plate and impermeable walls. The porous plate has a length of 581 mm. The channel has an open exit section that is connected to the ambient air. The channel height was adjusted to 10.3 mm. Cold air at 303 K is injected with a uniform mass flow rate, $2.619 \text{ kg/m}^2/\text{s}$, through the porous material. In the exit section the pressure is 1.374 bar in accordance with the operating of the experimental setup. Experimental setup and grids used for this test case is given in Figure 4.30 and Figure 4.31, respectively.

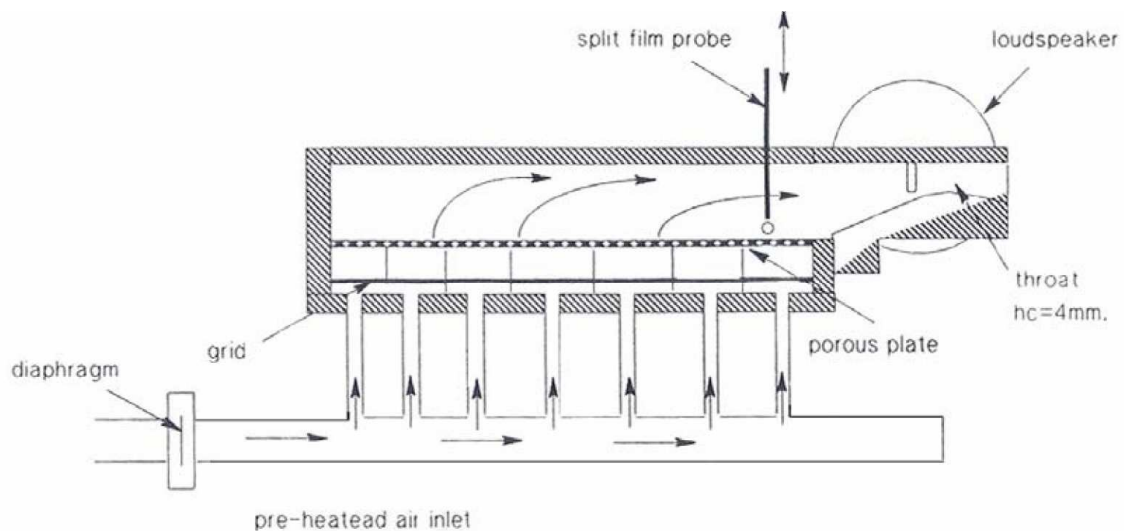


Figure 4.30 VECLA setup

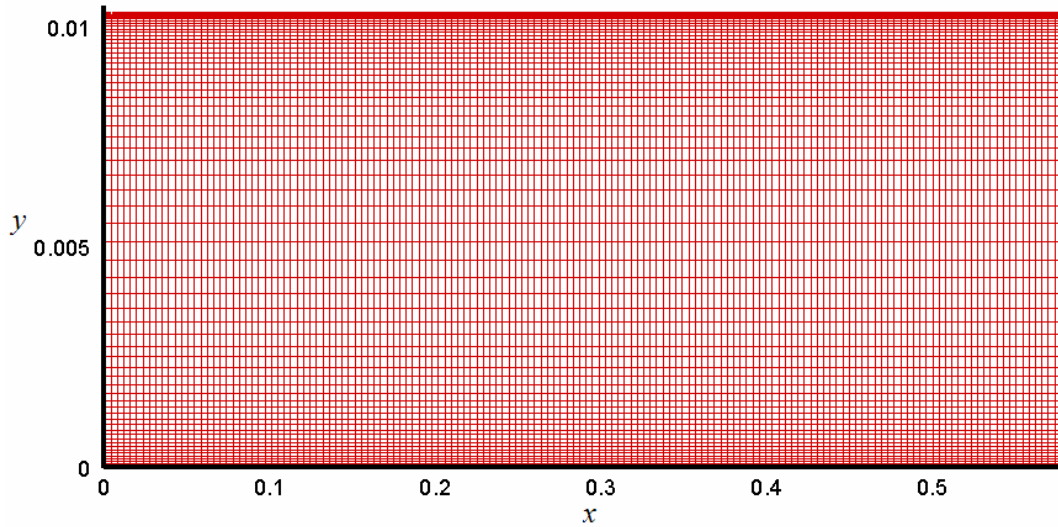


Figure 4.31 Grid used for the turbulent flow with mass injection

The results of this case are compared with the results taken from reference [34]. Axial velocity profiles along the y axis at different locations are given in Figure 4.32, Figure 4.33, Figure 4.34, Figure 4.35, Figure 4.36, Figure 4.37 and Figure 4.38. Solver developed by Onera is used for the results of $k-w$ method. Results of $k-\varepsilon$ method are obtained by using the solver developed by Roketsan. Computed turbulence profiles are suited with experimental data as the results of the $k-w$ and $k-\varepsilon$ methods obtained from the reference [34].

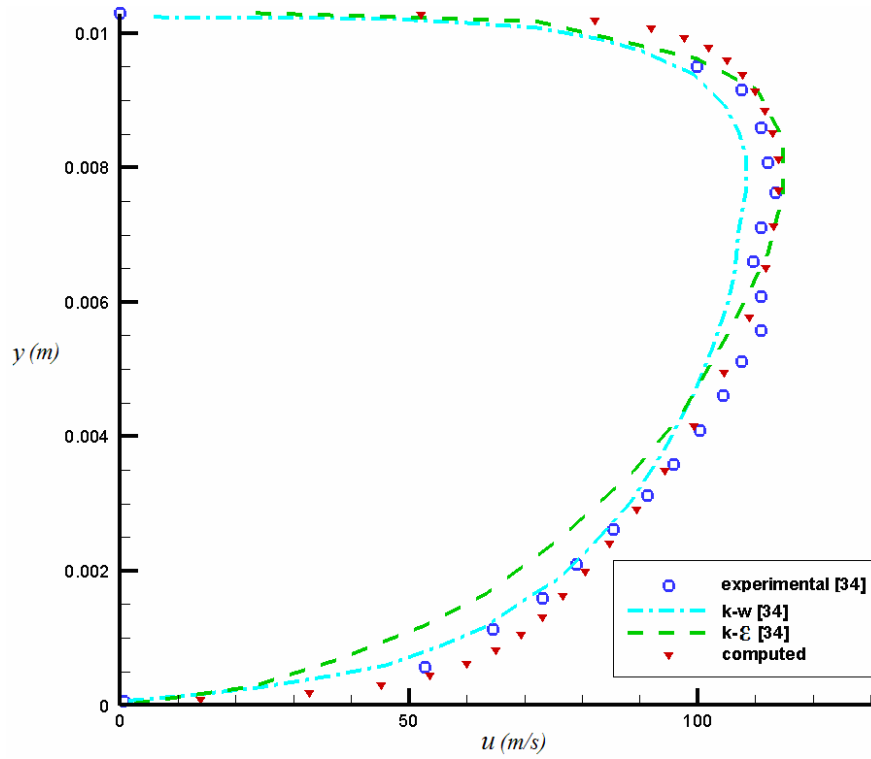


Figure 4.32 Axial velocity profiles at $x = 0.570$ m.

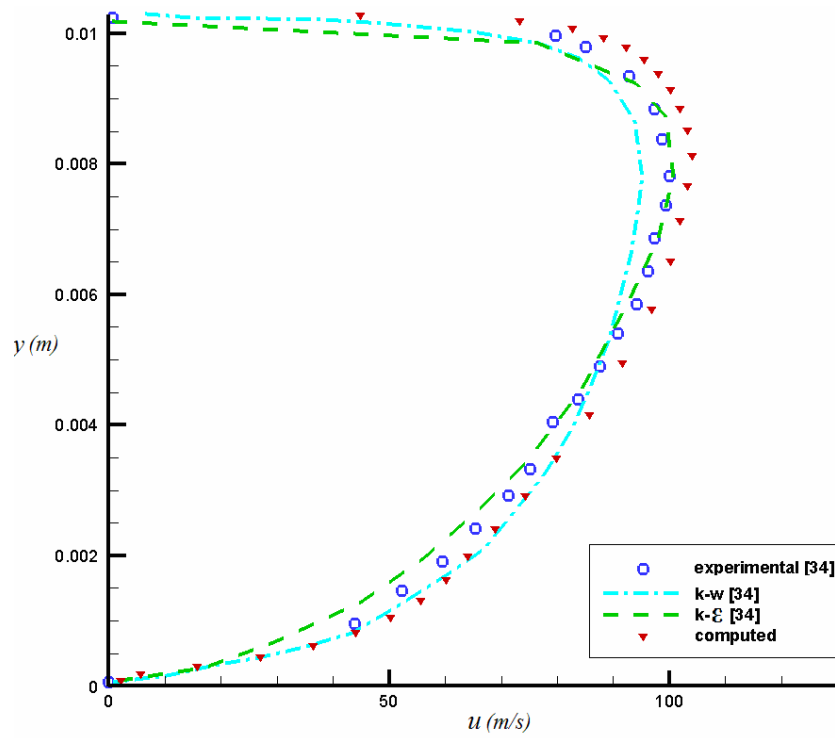


Figure 4.33 Axial velocity profiles at $x = 0.500$ m.

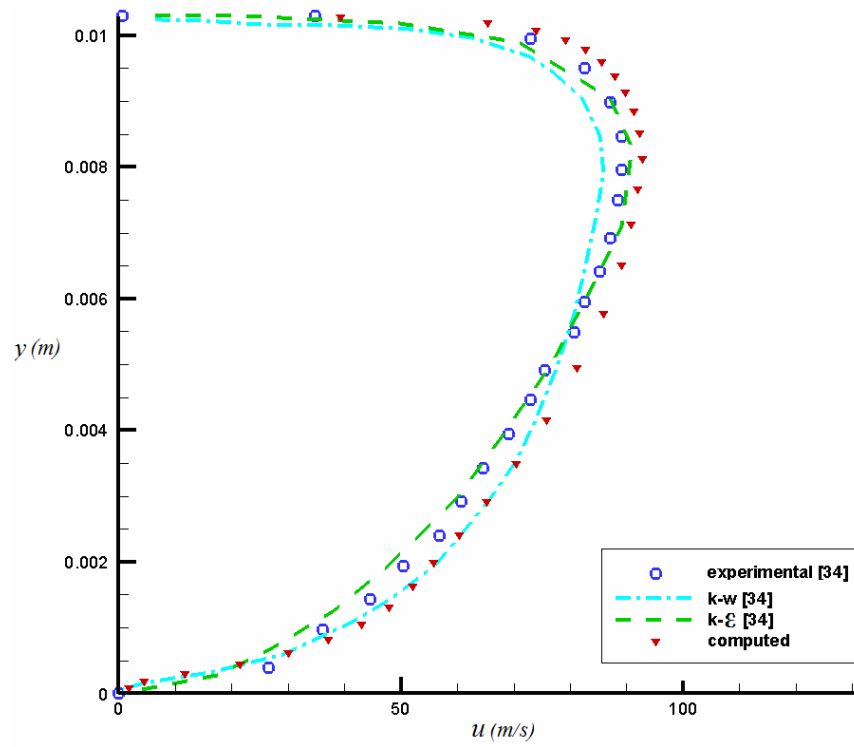


Figure 4.34 Axial velocity profiles at $x = 0.450$ m.

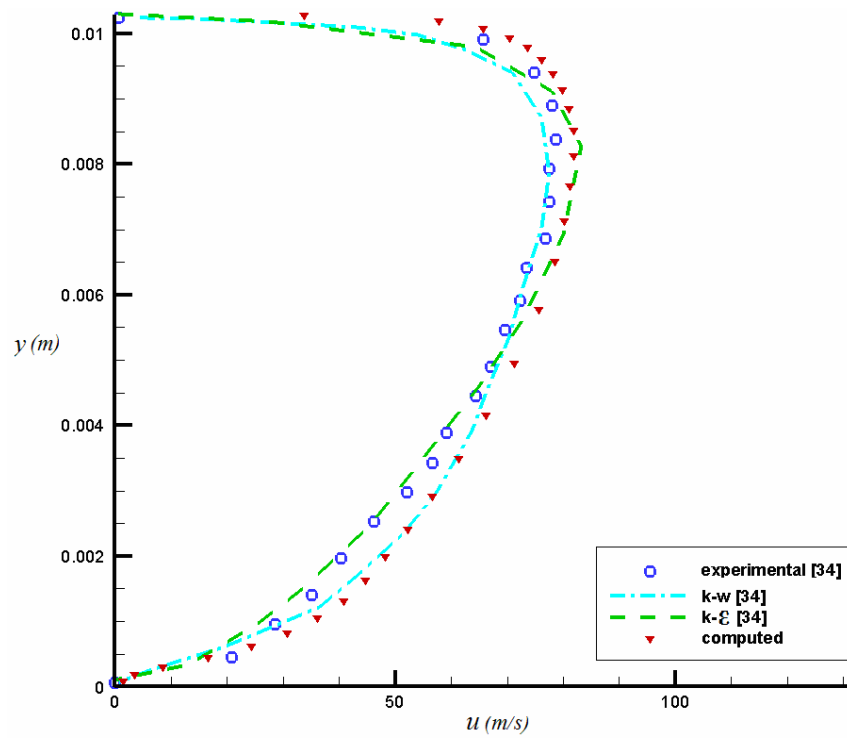


Figure 4.35 Axial velocity profiles at $x = 0.400$ m.

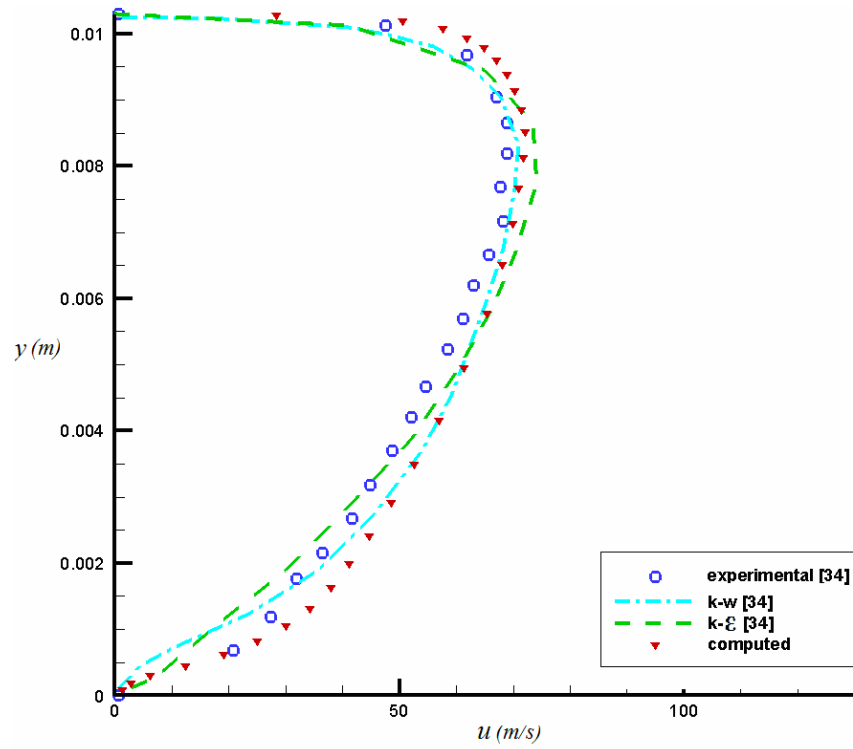


Figure 4.36 Axial velocity profiles at $x = 0.350$ m.

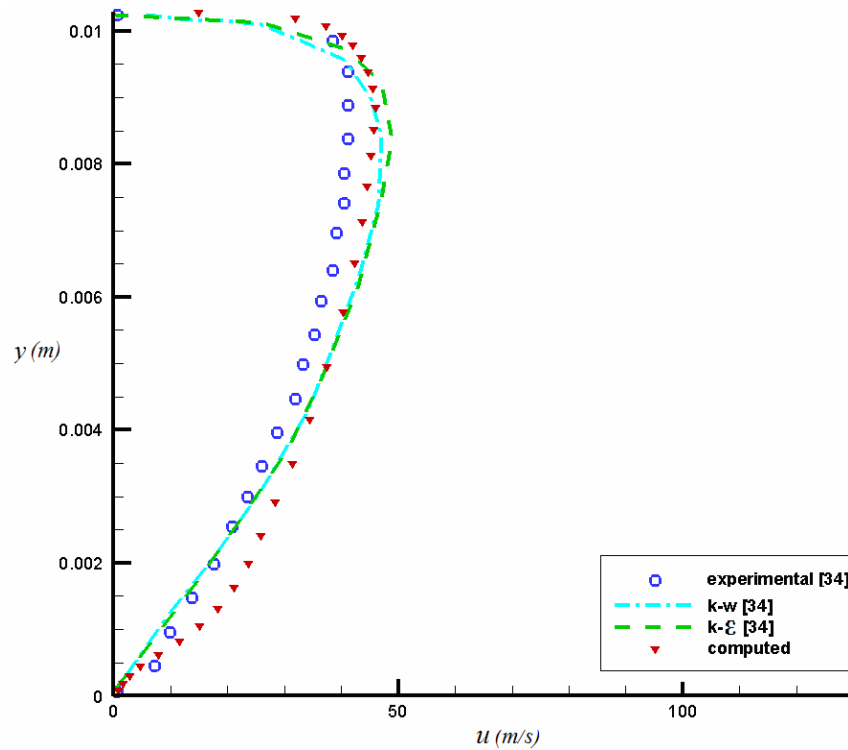


Figure 4.37 Axial velocity profiles at $x = 0.220$ m.

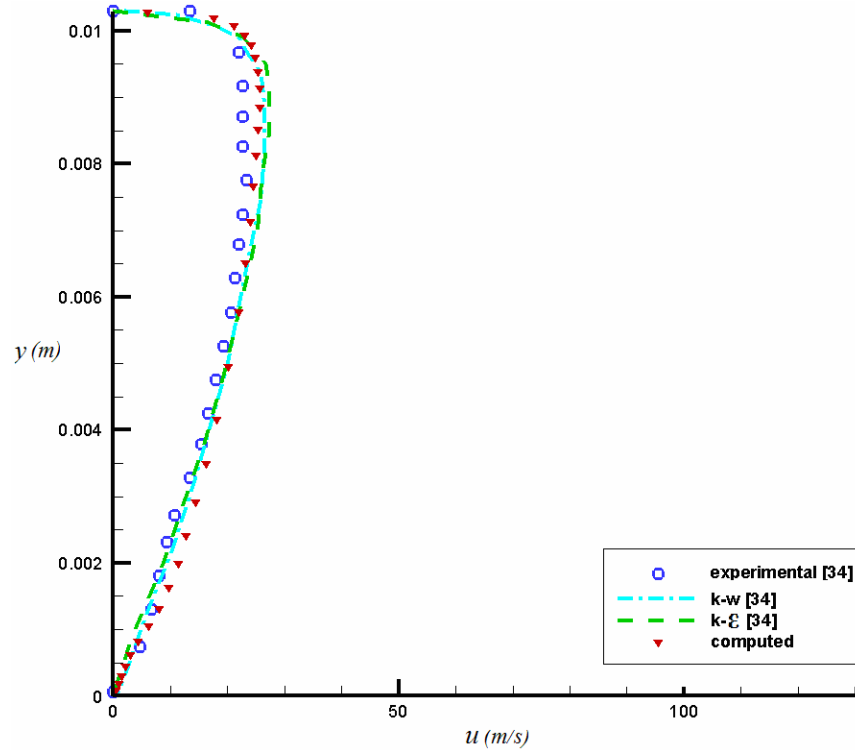


Figure 4.38 Axial velocity profiles at $x = 0.120$ m.

Laminar and turbulent results are compared with analytic laminar solutions which are given as [34]

$$\frac{u}{u_{inj}} = \frac{x}{h} \frac{\pi}{2} \cos\left(\frac{\pi y}{2h}\right) \quad (4.9)$$

where u represents axial velocity, u_{inj} represents injection gas velocity, h represents the height of the channel. Laminar results are approximately the same with the analytical solutions. Difference between the turbulent and laminar flows can be seen in the figure belows. Laminar results are well suited with the analytical solutions.

Axial velocity profiles at different location for laminar and turbulent flows are given in Figure 4.39, Figure 4.40, Figure 4.41, Figure 4.42, Figure 4.43 and Figure 4.44.

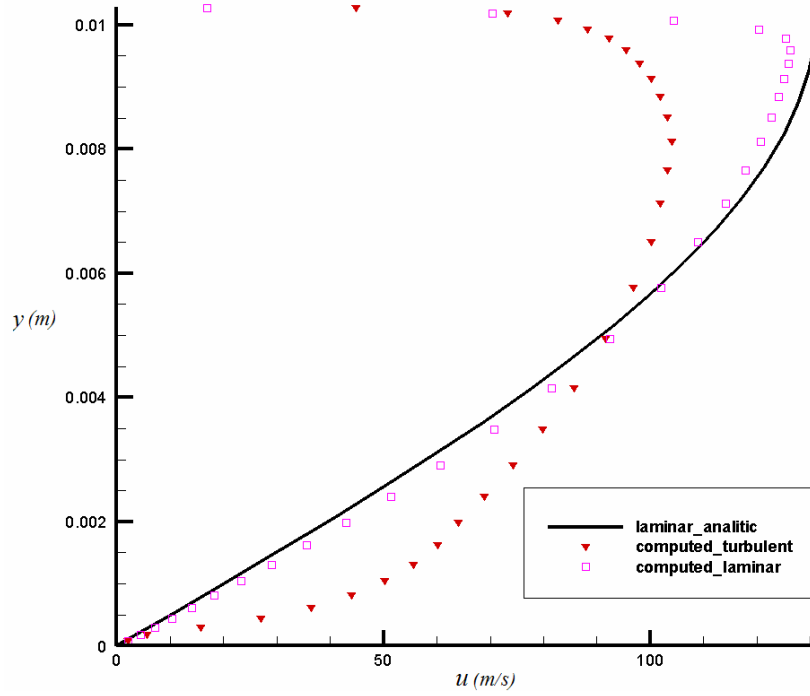


Figure 4.39 Analytical and computed axial velocity profiles at $x = 0.500$ m for laminar and turbulent flows.

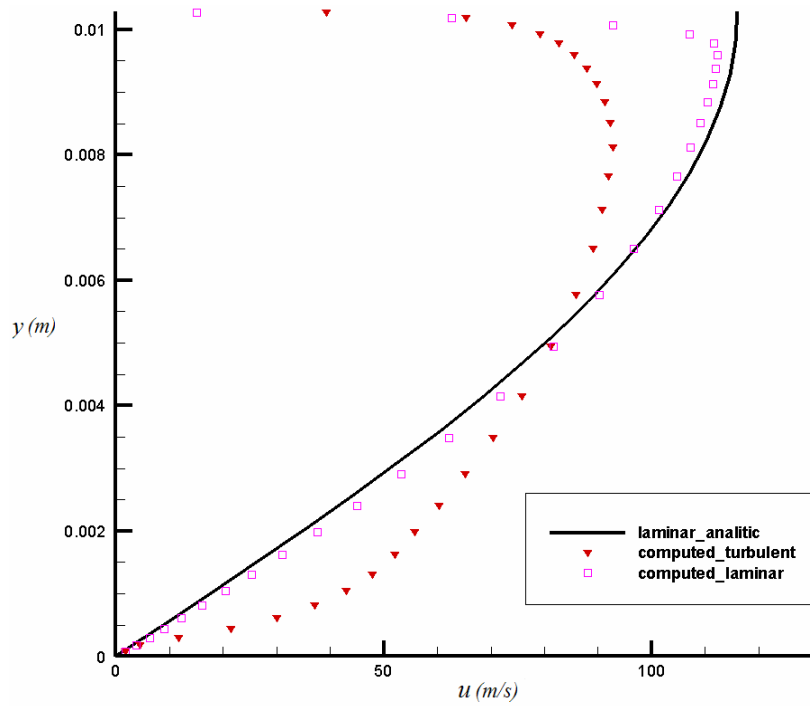


Figure 4.40 Analytical and computed axial velocity profiles at $x = 0.450$ m for laminar and turbulent flows.

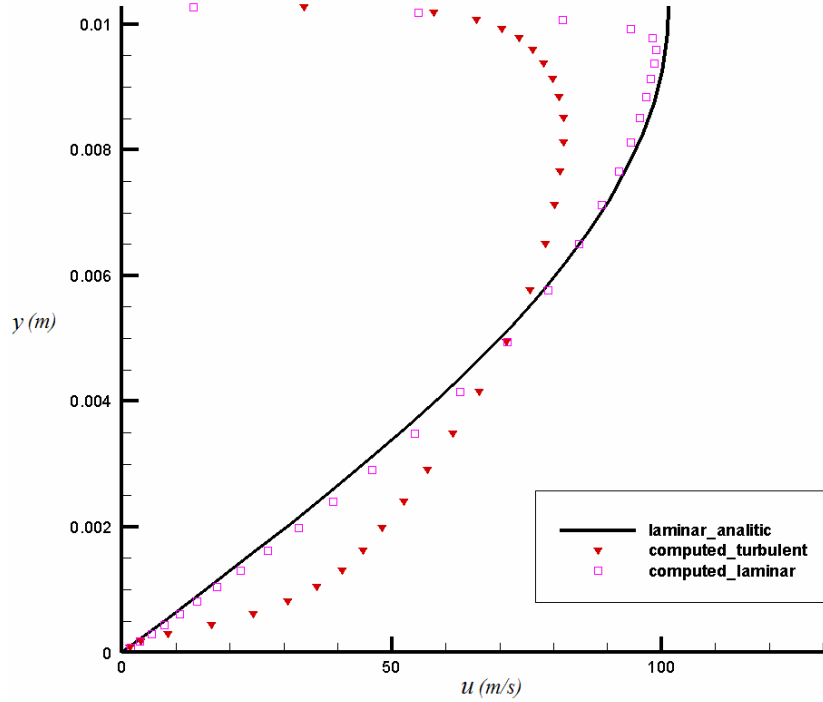


Figure 4.41 Analytical and computed axial velocity profiles at $x = 0.400$ m for laminar and turbulent flows.

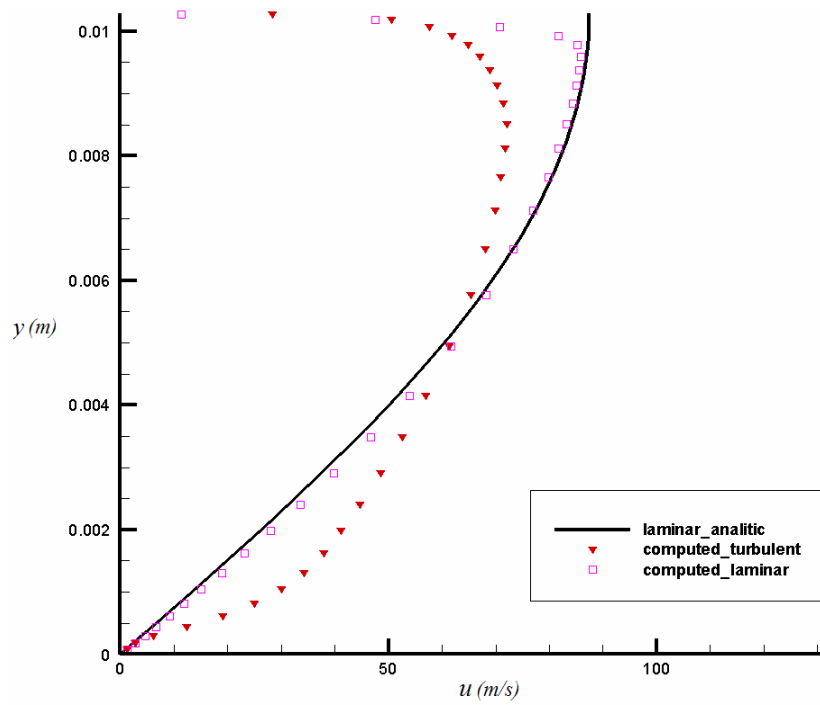


Figure 4.42 Analytical and computed axial velocity profiles at $x = 0.350$ m for laminar and turbulent flows.

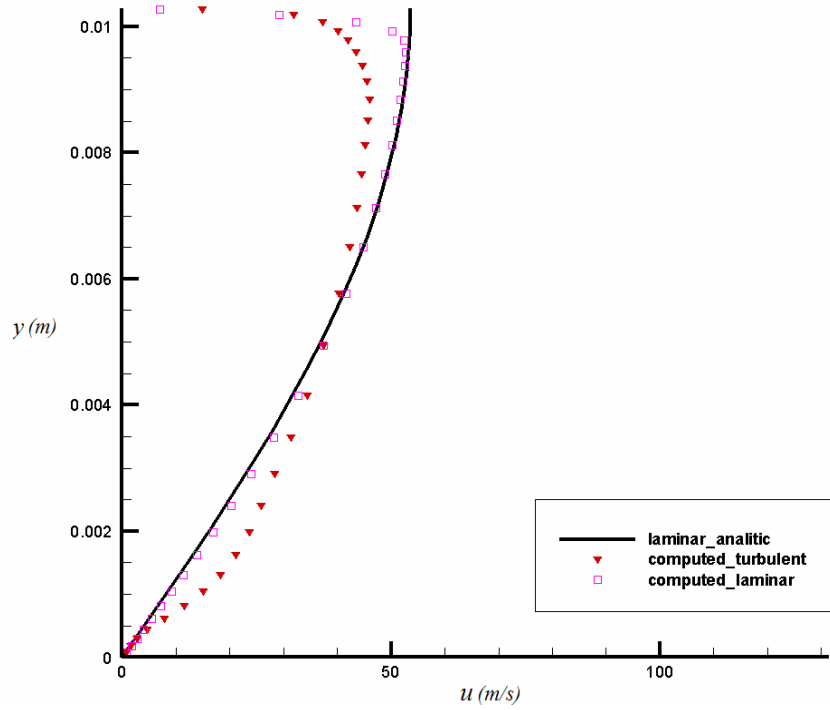


Figure 4.43 Analytical and computed axial velocity profiles at $x = 0.220$ m for laminar and turbulent flows.

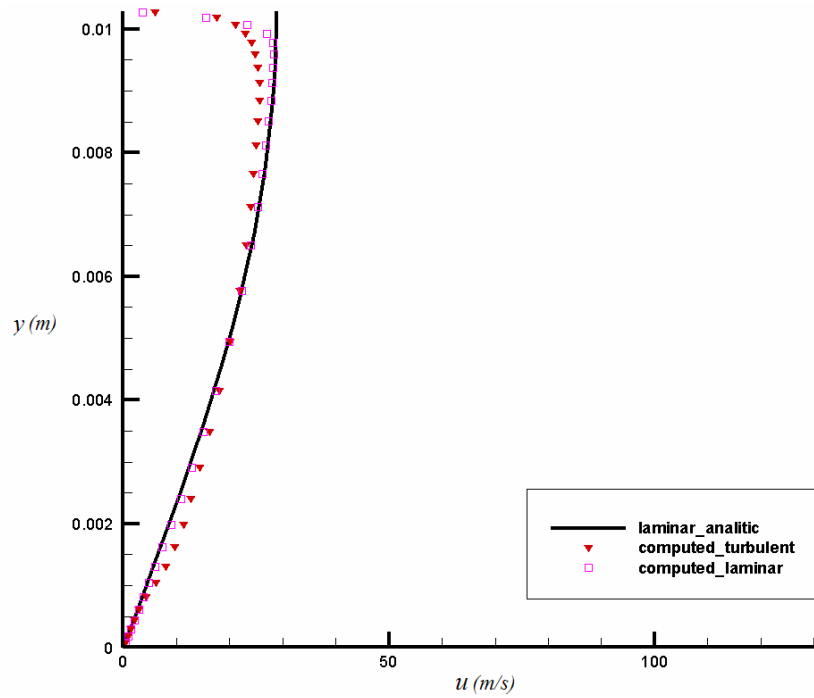


Figure 4.44 Analytical and computed axial velocity profiles at $x = 0.120$ m for laminar and turbulent flows.

CHAPTER 5

CONCLUSION

An explicit algorithm has been developed for the solution of Navier-Stokes equations on unstructured grids to model the axisymmetric, steady, turbulent flows. The developed solver can handle internal and external flows.

Convective fluxes were calculated by using the flux difference splitting methods. HLL and HLLC approximate Riemann solvers are used in the finite volume discretisation of the governing equations. Unstructured mesh can be used by developed code. Second order accuracy in space is achieved by piecewise linear reconstruction method. Green-Gauss method is used to compute the gradients of flow variables. Venkatakrisshnan's limiter is used for second order accurate solutions. Baldwin-Lomax turbulence model was used to model the turbulence effects in flows.

For the validation of the solver, six different test cases including cylindrical explosion, flow over a circular bump, axisymmetric flow in SPRM, laminar and turbulent flows over a flat plate and turbulent flow with mass injection. Cylindrical explosion case has been solved by using two different grids, unstructured quadrilateral and hybrid grids. Turbulent flow with mass injection case has been solved by using structured and unstructured hybrid mesh. For all case, the results are in good agreement with the reference data or analytical solution. Turbulent flow with mass injection case has been also compared by the experimental data.

Because of using the explicit temporal discretization method, solver converges slowly. For future developments, implementation of an implicit temporal discretization may be a course of action. Also higher order reconstruction scheme may be implemented in the solver. Also extension to three dimensions may be the continuation of this work.

REFERENCES

- [1] Tinaztepe, H., T., “A Finite Volume Method Compressible Viscous Flows”, *Ph. D. Thesis in Mechanical Engineering*, Middle East Technical University, 1997.
- [2] Frink, N. T., “Upwind Scheme for Solving the Euler Equations on Unstructured Grids”, *AIAA Journal Vol. 30*, No. 1, pp. 70-77, January, 1992.
- [3] Steger, J. L., and Warming, R. F., “Flux Vector Splitting of the Inviscid Gas Dynamics Equations with Applications to Finite Difference Methods”, *Journal of Computational Physics*, Vol. 40, pp. 263-293, 1981.
- [4] Blazek, J., “*Computational Fluid Dynamics: Principles and Applications*”, 1st Edition, Elsevier, 2001.
- [5] Van Leer, B., “Flux-Vector Splitting for the Euler Equations”, *Proc. 8th Int. Conf. on Numerical Methods in Fluid Dynamics*, Springer Verlag, 1982, pp. 507-512.
- [6] M-S. Liou, “A Sequel to AUSM, Part I: AUSM⁺”, *Journal of Computational Physics*, 129:364-482, 1996.
- [7] Godunov, S. K., “A Difference Method for the Numerical Computation of Discontinuous Solutions of Hydrodynamic Equations”, *Math Sbornik*, Vol. 47, pp. 271-306, 1959.
- [8] Roe, P. L., “Discrete Models for the Numerical Analysis of Time-Dependent Multidimensional Gas Dynamics”, *Journal of Computational Physics*, Vol. 63, pp. 458-476, 1986.

- [9] Osher, S., and Solomon, F., “Upwind Schemes for Hyperbolic Systems of Conservation Laws”, *Mathematics of Computation*, Vol. 38, No. 158, pp. 339-377, 1982.
- [10] Toro, E. F., “*Riemann Solvers and Numerical Methods for Fluid Dynamics*”, 1st Edition, Springer, 1997.
- [11] Harten, A., “High Resolution Schemes for Hyperbolic Conservation Laws”, *Journal of Computational Physics*, Vol. 49, pp. 357-393, 1983.
- [12] B. Van Leer A. Harten, P. D. Lax., “On Upstream Differencing and Godunov-Type Schemes for Hyperbolic Conservation Laws”, *SIAM Review*, 25(1):35–61, 1983.
- [13] S.F. Davis, “Simplified Second-Order Godunov-Type Methods”, *SIAM Journal on Scientific Statistical Computing*, 9:445–473, 1988.
- [14] B. Einfeldt., “On Godunov-Type Methods for Gas Dynamics”, *SIAM Journal on Numerical Analysis*, 25(2):294–318, 1988.
- [15] Mingham C. G. and Causon D. M., “High-Resolution Finite-Volume Method for Shallow Water Flows”, *J. Hydraulic Eng.*, 124(6), pp.605–614 (1998).
- [16] Hu K., Mingham C. G. and Causon D. M., “A Bore-Capturing Finite Volume Method for Open-Channel Flows”, *Int. J. Numer. Meth. Fluids*, 28, pp. 1241–1261 (1998).
- [17] Wackers J., Koren B., “Five Equation Model for Compressible Two Flow”, *Centrum voor Wiskunde en Informatica*, Report MAS-E0414, 2004.
- [18] Toro E. F., Spruce M., and Speares W., “Restoration of Contact Surface in the HLL-Riemann Solver”, *Shock Waves*, 4:25-34, 1994.

- [19] Batten P., Goldberg U. C., and Leschziner M. A., “Average-State Jacobians and Implicit Methods for Compressible Flows”, *Journal of Computational Physics*, Volume 137, No:1, 1997.
- [20] Wilcox D., C., “*Turbulence Modeling for CFD*”, Second Edition, DWC Industries Inc., 1993.
- [21] Schlichting, H., “*Boundary-Layer Theory*”, McGraw-Hill Book Company, 5th Edition, 1987.
- [22] Baldwin B.S. and Lomax H., “Thin-Layer Approximation and Algebraic Model for Separated Turbulent Flows”, *AIAA Paper*, 78– 257, 1978.
- [23] Hirsch, C., “*Numerical Computation of Internal and External Flows*”, Vol 1&2, John Wiley&Sons, 1989.
- [24] C. Lambert P. Batten, N. Clarke and D. M. Causon, “On the Choice of Wave Speeds for HLLC Riemann Solvers”, *SIAM Journal on Scientific Computing*, 18:1553–1570, 1997.
- [25] Venkatakrishnan, V., “On the Accuracy of Limiters and Convergence to Steady State Solutions”, *AIAA Paper 93-0880*, 1993.
- [26] M-S. Liou, “A Sequel to AUSM, Part II: AUSM⁺ Up for All Speeds”. *Journal of Computational Physics*, 214:137–170, 2006.
- [27] K. Segeth P. Solin, Linz, “Description of Multi-Dimensional Finite Volume Solver EULER”. *Application of Mathematics*, 47(2):169–185, 2002.
- [28] S. T. Yu, “Convenient Method to Convert Two-Dimensional CFD Codes into Axisymmetric Ones”. *Journal of Propulsion and Power*, 9(3):493– 495, May-June, 1993.

- [29] Kalpaklı, B., “Development of Multi-Dimensional Hydrocode Solver with Diffuse Interface”, *Ph.D. Thesis Progress Report in Engineering Science*, Middle East Technical University, 2009.
- [30] Ni, R. H., “A Multiple-Grid Scheme for Solving the Euler Equations”, *AIAA 137 Journal*, Vol. 20, pp. 1565-1571, 1982.
- [31] Yumuşak M., Taşkınoğlu E., and Tınaztepe T., “ 2-D Internal Flow Applications for Solid Propellant Rocket Motors”, *Technical Report of NATO-RTO T108 Support Project*, 1999.
- [32] Avalon G., Casalis G., Griffond J., “Flow Instabilities and Acoustic Resonance of Channels with Wall Injection”, *AIAA Paper 98-3218, AIAA 34th Joint Propulsion Conference, Cleveland*, July 13-15, 1998.
- [33] Casalis G., Avalon G., Pineau J.Ph., “Spatial Instability of Planar Channel Flow with Fluid Injection Through Porous Walls”, *Physics of Fluid*, Vol. 10, No. 10, pp. 2558-2568, 1998.
- [34] Yumuşak M., Erdoğan E., and Tınaztepe T., “ Viscous Internal Flow Applications for Solid Propellant Rocket Motors”, *Technical Report of NATO-RTO-AVT T124 Support Project*, 2005.